Tectonics

RESEARCH ARTICLE
10.1029/2020TC006246

Key Points:
- Data are interpretable in terms of age-deformation relationships and capture a broad-scale localization of strain in time and space
- At smaller scale, relating age with structures is more difficult because of greater complexity in $^{40}Ar/^{39}Ar$ systematics
- The shear zone has a duration of ~12 Myr during exhumation and deformation ended in the upper part of the viscous/brittle transition

Supporting Information:
- Supporting Information S1
- Table S1
- Table S2
- Table S3

Correspondence to:
A. Beaudoin,
alexandre.beaudoin@univ-orleans.fr

Citation:
Beaudoin, A., Scaillet, S., Mora, N., Jolivet, L., & Augier, R. (2020). In situ and step-heating $^{40}Ar/^{39}Ar$ dating of white mica in low-temperature shear zones (Tenda massif, Alpine Corsica, France). *Tectonics*, *39*, e2020TC006246. https://doi.org/10.1029/2020TC006246

Received 13 APR 2020
Accepted 23 OCT 2020
Accepted article online 31 OCT 2020

In Situ and Step-Heating $^{40}Ar/^{39}Ar$ Dating of White Mica in Low-Temperature Shear Zones (Tenda Massif, Alpine Corsica, France)

Alexandre Beaudoin[1,2,3], Stéphane Scaillet[1,2,3], Nicolas Mora[1,2,3], Laurent Jolivet[4], and Romain Augier[1,2,3]

[1]Université d'Orléans, ISTO, UMR 7327, Orléans, France, [2]CNRS/INSU, ISTO, UMR 7327, Orléans, France, [3]BRGM, ISTO, UMR 7327, Orléans, France, [4]CNRS/INSU, ISTeP, UMR 7193, Sorbonne Université, Paris, France

Abstract In order to clarify the link between $^{40}Ar/^{39}Ar$ record in white mica and deformation, we performed in situ and bulkwise $^{40}Ar/^{39}Ar$ dating over the East Tenda Shear Zone (Tenda massif, Alpine Corsica). White micas from 11 samples were selected and extensively analyzed using in situ techniques across nested scales of strain-intensity gradients developed at the expense of a late-Variscan protolith. $^{40}Ar/^{39}Ar$ systematics are unaffected by inherited Ar and directly linked to deformation with little or no Ar lattice (volume) diffusion. Extensive sampling allows constraining the end of deformation related to burial and exhumation, respectively, at ~34 and ~22 Ma, bracketing the duration of regional extensional shear to ~12 Myr. Results also highlight a regional strain localization toward the upper contact of the unit with smaller-scale localization in specific lithologies, notably meta-aplites. Second-order complications exist, such as local ill-defined correlations between ages and finite-strain microstructures. Thus, the use of a strain gradient as a proxy for strain localization in time is regionally valid but sometimes locally too complex to track or resolve strain partitioning/localization trends at the meter (outcrop) scale and below. Age mixing and incomplete isotopic homogenization by dissolution/precipitation are identified as the main causes of local discrepancies that complicate the link between age and microstructure and the derivation of strain localization rates. Tracking temporal trends in shear distribution across regional-scale deformation gradients in such settings is possible but requires a multi-scale approach as implemented here to reveal younging patterns associated to strain localization.

1. Introduction

The significance of $^{40}Ar/^{39}Ar$ ages in deformed rocks has been the focus of many studies since 1990. A central motivation of such studies is the potential of the $^{40}Ar/^{39}Ar$ dating to provide (i) temporal control on deformation structures and crustal shear zones (e.g., Brunet et al., 2000; Di Vincenzo et al., 2016; Isik et al., 2004; Kligfield et al., 1986; Rolland et al., 2013; Turrillot et al., 2011), (ii) determine and correlate the sequence of events in polydeformed rocks (e.g., Augier et al., 2005; Beltrando et al., 2009; Castonguay et al., 2007; Condon et al., 2006; Hames & Cheney, 1997), and (iii) infer the kinematics, evolution, and partition of shear in tectonic systems undergoing progressive deformation (e.g., Bellanger et al., 2015; Cardello et al., 2019; Dunlap et al., 1991; Kellett et al., 2016; Rolland et al., 2009; Sanchez et al., 2011; Schneider et al., 2013; West & Hubbard, 1997). Practically, the question of dating deformation in such contexts is whether or not the $^{40}Ar/^{39}Ar$ targets (typically micas) can actually record deformation as a result of structural-stoichiometric recombination (recrystallization and neoblastesis) and whether these phenomena are kinetically more efficient than temperature for Ar exchange and resetting (e.g., Di Vincenzo et al., 2001, 2004, 2006; Scaillet et al., 1992). Several works have emphasized that isotopic closure by cooling is prevalent when peak-metamorphic conditions during deformation are hot enough to cause the system to close after the syn-kinematic fabric has developed, resulting in closure ages potentially decoupled from the deformation itself (Goodwin & Renne, 1991; Markley et al., 2002; Mulch et al., 2002; Mulch & Cosca, 2004; Scharf et al., 2016).

The case of white mica is particularly emblematic of such issues. Its ^{40}Ar retention kinetics have been empirically (Hames & Bowring, 1994; Kirschner et al., 1996) and experimentally (Harrison et al., 2009) found to straddle the viscous/brittle transition in mid-crustal levels (330–450°C) across which many

fabrics targeted for $^{40}Ar/^{39}Ar$ dating develop. Forming solid solutions with several end-members, white mica is also stable across a wide range of *P-T* variations in a large variety of lithologies. This potentially induces coupled Ar-structural-stoichiometric changes according to the *P-T-t-strain* path undergone by the host rock and the time spent through the transitional ^{40}Ar retention zone while the fabric dynamically develops (e.g., Di Vincenzo et al., 2001; Putlitz et al., 2005; Scaillet et al., 1992). Such a record is reflected in complex major-elements and $^{40}Ar/^{39}Ar$ variations that have defied attempts at extracting useful geochronologic information from such data (e.g., Di Vincenzo et al., 2001, 2006; Scaillet, 1998). The problems fundamentally raised by such systems may be stated as follows (see review in Scaillet, 1998, and Di Vincenzo et al., 2006; Smye et al., 2013; Warren et al., 2012):

1. How well are ^{40}Ar mica diffusion rates constrained and how do these interact with *P-T-t* induced crystallographic changes, either dynamic or static?
2. Which are the mechanisms involved at the crystallographic scale and how do they relate with lithology, rheology, and strain partitioning in a strain gradient?
3. How does kinetic hindrance and transformation rates affect the $^{40}Ar/^{39}Ar$ record as a function of starting mineralogy and associated rheology?
4. How does the catalytic action of metamorphic fluids combine with solid-state processes during fluid/solid interactions?

The cocktail of physics implied by such phenomena is common to natural systems, inducing complex feedback relationships between mineralogy, rheology, reactivity, fluid flow, metasomatism, and transient permeability. This has so far impaired the establishment of universal guidelines to interpret $^{40}Ar/^{39}Ar$ white mica ages in shear zones (see review in Oriolo et al., 2018), to a large extent undermining their constraining power for quantitative modeling of thermo-mechanical and rheological processes.

In this study, we tackle the problem the other way round. Barring a satisfactory calibration of the physical parameters collectively involved through (1) and (4) above, we simplify the problem by studying a pre-kinematic intrusion, that is,

1. spatially homogeneous in terms of starting protolith with a regionally coherent *P-T-t* evolution,
2. sufficiently old to enhance the Ar isotopic contrast with newly grown syn-kinematic micas,
3. spatially heterogeneous in finite-strain pattern to allow the effects of variable deformation to be examined.

Our target is the Tenda massif in Alpine Corsica (France), a regionally sized coherent unit belonging to the European margin buried and later exhumed during the Apulia-Adria convergence. The massif consists of a ~290 Ma late-Variscan composite intrusion (Rossi et al., 1993) that was extensively yet heterogeneously reworked during the Alpine orogeny (Daniel et al., 1996; Gueydan et al., 2017; Jolivet et al., 1990, 1991; Jourdan, 1988; Maggi et al., 2012, 2014; Mattauer et al., 1981; Molli et al., 2006; Molli & Malavieille, 2011; Molli & Tribuzio, 2004; Rossetti et al., 2015). Large-scale geometry, kinematics, and strain gradients have been recently studied (Beaudoin et al., 2017) along with the regional *P-T* evolution (Maggi et al., 2012; Molli et al., 2006; Molli & Tribuzio, 2004; Tribuzio & Giacomini, 2002), while recent Rb-Sr ages can be used to independently constrain spatial-temporal crystallization patterns (Rossetti et al., 2015).

Our strategy combines extensive $^{40}Ar/^{39}Ar$ dating with systematic microstructural and petrological characterization of white mica sampled along major and small-scale strain gradients recognized and mapped through the massif (Beaudoin et al., 2017). By using complementary in situ and step-heating techniques, we document and explore the link between age, grain size, chemical composition, and attempt to relate them to multi-scale strain gradients and structures.

2. Geological Setting

2.1. Regional-Scale Nappe Structure of Alpine Corsica

The Tenda massif belongs to Alpine Corsica (Figure 1), a Cenozoic stack of tectono-metamorphic units forming a westward-verging H*P*-L*T* subduction wedge overthrust on the autochthonous crystalline basement of Variscan Corsica (e.g., Caron, 1994; Fournier et al., 1991; Lahondère, 1988; Mattauer et al., 1981; Vitale Brovarone et al., 2013). In this wedge, the Tenda massif corresponds to the distal continental European

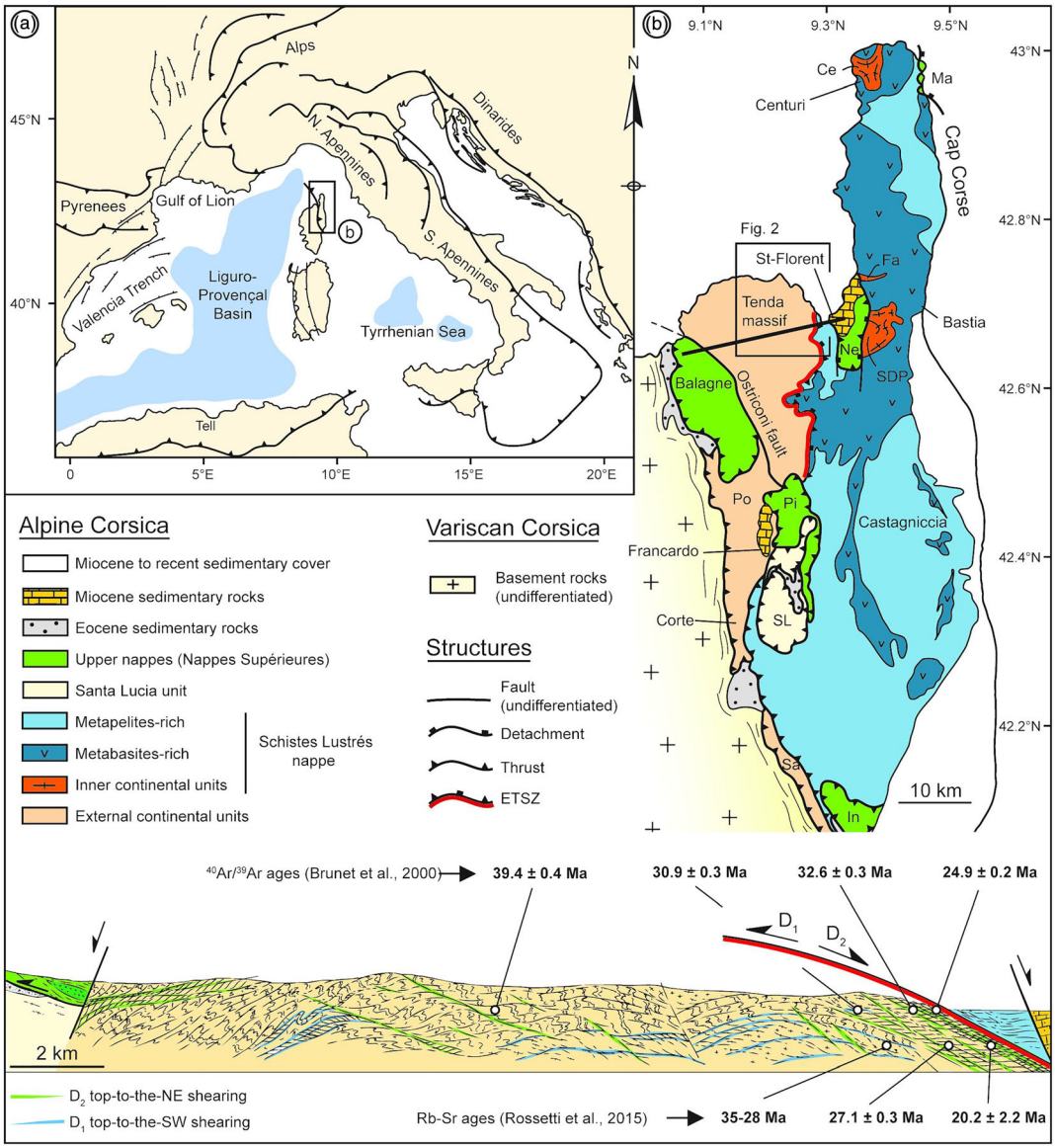

Figure 1. Geological context of the studied area. (a) Tectonic map of the western Mediterranean region. (b) Geological map of Alpine Corsica (modified after Vitale Brovarone et al., 2013) associated with a representative cross-section of the Tenda massif (modified after Beaudoin et al., 2017). Previous $^{40}Ar/^{39}Ar$ and Rb-Sr ages are projected on the cross section. Ce: Centuri continental unit; Fa: Farinole continental unit; In: Inzecca unit; Ma: Macinaggio unit; Ne: Nebbio unit; Sa: Sampolo unit; SDP: Serra di Pigno continental unit; SL: Santa Lucia; Pi: Pineto ophiolitic unit; Po: Popolasca unit.

margin involved in subduction down to blueschist-facies conditions (Gibbons & Horak, 1984; Maggi et al., 2012; Molli & Tribuzio, 2004; Tribuzio & Giacomini, 2002; Vitale Brovarone et al., 2013). It is bounded to the east by the East Tenda Shear Zone (ETSZ; Figure 1), that puts it in contact structurally below the Schistes Lustrés nappe, an internal ocean-derived unit of Ligurian affinity that recorded eclogite-facies conditions (Caron, 1994; Caron et al., 1981; Caron & Péquignot, 1986; Daniel et al., 1996; Fournier et al., 1991; Jolivet et al., 1990, 1991, 1998; Lahondère, 1988; Ravna et al., 2010; Vitale Brovarone, Groppo, et al., 2011; Vitale Brovarone, Beltrando, et al., 2011). To the west, it is separated by the Ostriconi fault (Figure 1) from the Nappes Supérieures of Balagne that essentially correspond to low-grade Jurassic ophiolites and Cretaceous flysch of Ligurian affinity (Beccaluva et al., 1981; De Wever et al., 1987; Ohnenstetter et al., 1981).

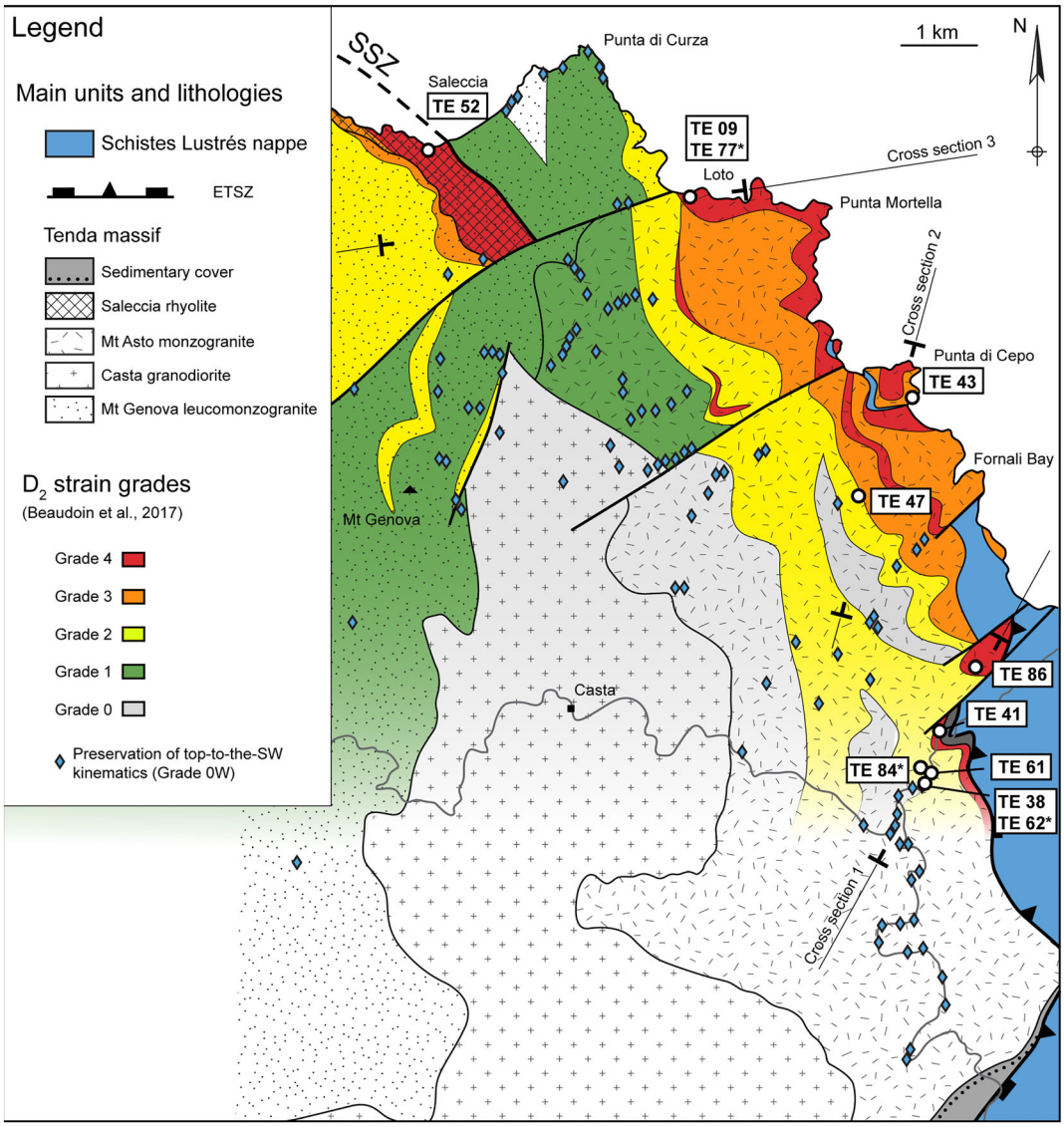

Figure 2. Deformation intensity map and samples location (modified after Beaudoin et al., 2017). The geological outlines in the background are from Rossi et al., (2001), Rossi, Lahondère et al. (1994) and Beaudoin et al. (2017). Cross sections presented in Figures 8–11 (step-heating results) are indicated. The asterisks indicate samples also dated by the in situ approach.

2.2. Tectonometamorphic Evolution of the Tenda Massif

The Tenda massif consists of a Variscan basement portion overlain by a Meso-Cenozoic sedimentary cover (Figure 2; Jourdan, 1988; Rossi et al., 2001; Vitale Brovarone et al., 2013). Its western part is represented by Proterozoic to Paleozoic gneisses and micaschists unconformably overlain by late-Variscan volcano-sedimentary rocks. The eastern part consists of late-Carboniferous/early-Permian granite intrusions (Rossi, Lahondère et al. 1994, Rossi et al., (1993) including, from east to west: the Mt. Asto monzogranite, the Casta granodiorite, and the Mt. Genova leuco-monzogranite. Few sub-volcanic facies such as the Saleccia rhyolite are also present (Beaudoin et al., 2017).

The finite structure of the Tenda massif is the result of polyphazed deformation. The first event (D_1) is associated with the development of a non-coaxial planar-linear fabric (S_1/L_1) with a predominant top-to-the-SW sense of shear coeval with burial under the Schistes Lustrés nappe down to blueschists-facies conditions (Beaudoin et al., 2017; Daniel et al., 1996; Gueydan et al., 2017; Jolivet et al., 1990, 1991; Jourdan, 1988;

Maggi et al., 2012, 2014; Mattauer et al., 1981; Molli et al., 2006; Molli & Malavieille, 2011; Molli & Tribuzio, 2004; Rossetti et al., 2015). Three models have been proposed for the post-D_1 evolution:

1. For Jolivet et al. (1990, 1991), Daniel et al. (1996), Gueydan et al. (2003), and Beaudoin et al. (2017), a D_2 event occurred mainly as a post-orogenic exhumation until semi-brittle conditions. A pervasive deformation reworked former structures. It includes D_2-folds and crenulation cleavages associated with a second planar-linear fabric (S_2/L_2) preserved in more coaxially deformed domains in between top-to-the-NE deformation zones. This deformation shows a large-scale strain gradient toward the core of the ETSZ (Figure 2; Beaudoin et al., 2017). The feldspar-to-phengite reaction is proposed to be the weakening mechanism responsible for strain localization (Gueydan et al., 2003).
2. According to Molli and Tribuzio (2004) and Molli et al. (2006), crenulation cleavages in the ETSZ may be partly interpreted as low-strained domains preserved between zones of localized top-to-the-SW shearing during D_1. D_2 is associated with the same structures as for the previous model, but is ascribed to syn-convergence exhumation of both the Schistes Lustrés nappe and the Tenda massif. This was accommodated by a basal top-to-the-SW shear zone below and a top-to-the-NE shear zone at the top of the coupled units, with an otherwise internal distributed deformation. The ETSZ was finally reactivated locally by top-to-the-NE shearing in a post-orogenic context and until brittle conditions at the end of exhumation (D_3).
3. Maggi et al. (2012, 2014) and Rossetti et al. (2015) also proposed that exhumation was mostly syn-orogenic but with a still active top-to-the-SW shearing in the ETSZ. Strain gradients from gneisses to phyllonites developed during this phase and are proposed to be due to transient rheology with softening due to feldspar-to-micas reaction and hardening by neoblastesis of alkali feldspar (albite porphyroclast rimmed by microcline) during fluid metasomatism. Only the final stages of exhumation are recorded during post-orogenic extension, where top-to-the-SW phyllonites are the only structures reactivated semi-brittlely by top-to-the-NE shearing.

H*P*-L*T* conditions are indicated by ubiquitous celadonite-rich phengite mineral assemblages locally including sodic blue amphibole (riebeckite-ferroglaucophane), jadeite-bearing aegirine or even clinopyroxene + rutile (Gibbons & Horak, 1984; Maggi et al., 2012; Molli et al., 2006; Molli & Tribuzio, 2004; Rossetti et al., 2015; Tribuzio & Giacomini, 2002). Corresponding peak-metamorphic conditions fall in the range of 0.8–1.2 GPa for 350–450°C (Maggi et al., 2012; Molli et al., 2006; Molli & Tribuzio, 2004), with maximum temperature rated at 360 ± 50°C from Raman spectroscopy on carbonaceous material in metasediments of the cover series (Vitale Brovarone et al., 2013). The retrograde path is characterized by an overall temperature decrease during exhumation running parallel to the phengite Si^{4+} isopleths and allowing the preservation of highly substituted phengites (Maggi et al., 2012).

2.3. Stratigraphic and Radiometric Constraints

Stratigraphic data (Figure 3) constrain the timing of events in the distal zones of the subduction wedge. In northern Corsica, metamorphism affects Bartonian sediments and is thus post-40 Ma (Bézert & Caby, 1988). Priabonian (34–37 Ma) sediments are either interpreted as post-metamorphism (Ferrandini et al., 2010) or pre-metamorphism (Bézert & Caby, 1989). Nappe emplacement occurred after 41 Ma, as shown by reworked Lutetian sediments under the Santa Lucia nappe (Rossi, Durand-Delga, et al., 1994; Ferrandini et al., 2010) and the Balagne nappe (Nardi et al., 1978). Toward more internal units, metamorphism in the Tenda massif is considered to be post-Paleocene (~53 Ma), as Eocene sedimentary rocks (dated by correlation with similar facies in Alpine Corsica) are affected by this metamorphism (Rossi et al., 2001). Finally, the orogenic wedge structure is unconformably overlain by the Middle Burdigalian (~18 Ma) extensional basins of Francardo and Saint-Florent, respectively, in internal and external positions (Cavazza et al., 2007; Ferrandini et al., 2003).

Radiometric constraints are quite controversial in Alpine Corsica (Figure 3). The youngest ages of H*P*-L*T* metamorphism in the Schistes Lustrés nappe are constrained between 37 and 34 Ma (U/Pb on zircon, Martin et al., 2011; Lu/Hf on garnet and lawsonite, Vitale Brovarone & Herwartz, 2013). These ages are consistent with a minimum H*P*-L*T* age of 34 Ma inferred by Brunet et al. (2000) from $^{40}Ar/^{39}Ar$ dating on phengite, with older ages up to ~60 Ma interpreted to reflect excess Ar. Taken at face value, the Upper Cretaceous age from Lahondère and Guerrot (1997) (Sm/Nd on whole rock, garnet, glaucophane, and clinopyroxene)

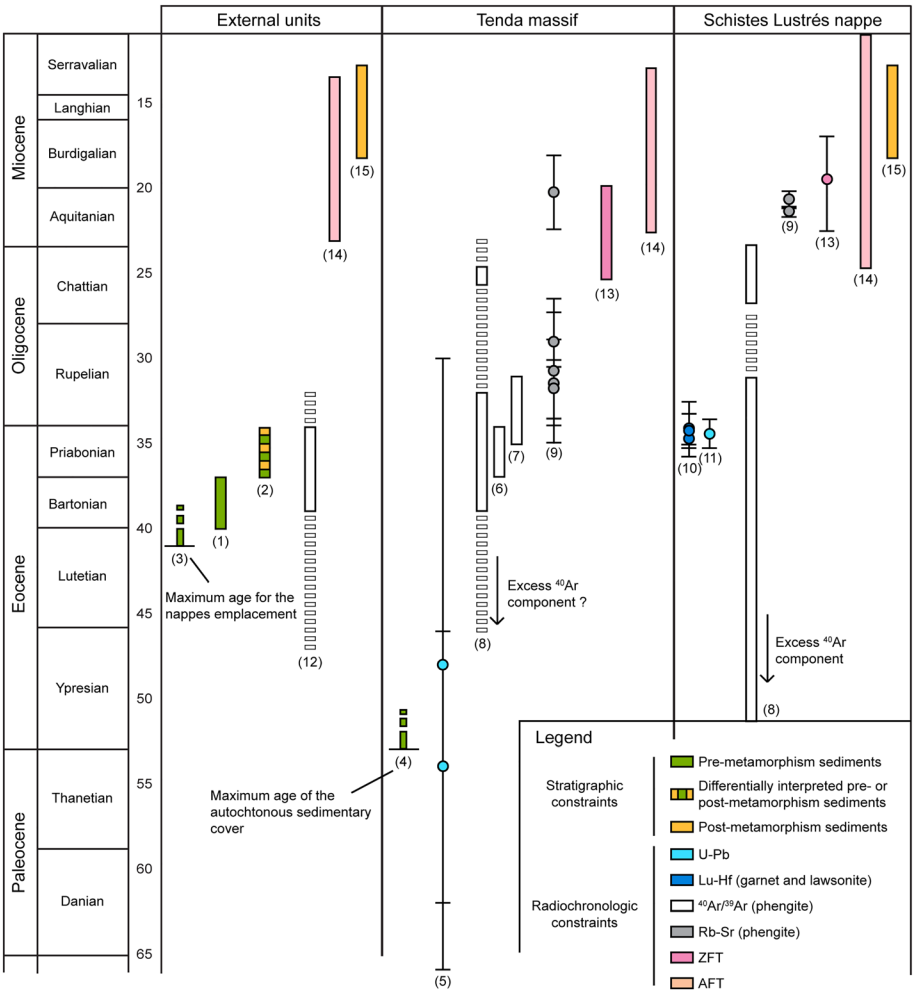

Figure 3. Biostratigraphic and radiometric constraints on tectonic and metamorphic events in Alpine Corsica. See text for further explanations. (1) Bézert and Caby (1988); (2) Bézert and Caby (1989) and Ferrandini et al. (2010); (3) Nardi et al. (1978), Rossi, Durand-Delga, et al. (1994), and Ferrandini et al. (2010); (4) Rossi et al. (2001); (5) Maggi et al. (2012); (6) Mailhé (1982); (7) Jourdan (1988); (8) Brunet et al. (2000); (9) Rossetti et al. (2015); (10) Vitale Brovarone and Herwartz (2013); (11) Martin et al. (2011); (12) Di Vincenzo et al. (2016); (13) Fellin et al. (2006); (14) Cavazza et al. (2001), Zarki-Jakni et al. (2004), and Danisik et al. (2007); (15) Ferrandini et al. (2003) and Cavazza et al. (2007).

appears questionable and problematic. Increments of exhumation are inferred from $^{40}Ar/^{39}Ar$ (Brunet et al., 2000), and Rb-Sr (Rossetti et al., 2015) ages on phengite around 25 and 20 Ma, respectively, and interpreted as crystallization ages during retrogressive shearing.

Accurate age constraints of H*P*-L*T* metamorphism in the Tenda massif are still lacking while existing radiometric data are scattered. In the ETSZ, the timing of prograde top-to-the-SW shear is constrained between 54 ± 8 Ma and 48 ± 18 Ma by U/Pb data from syn-kinematic rutile, coexisting acmite-phengite, and coatings of oxides or sulphides (Maggi et al., 2012). Late-Eocene/early-Oligocene $^{40}Ar/^{39}Ar$ phengite ages have been reported between 37 and 34 Ma, (Mailhé, 1982), and 35–31 Ma (Jourdan, 1988). These fall in the same range than in situ $^{40}Ar/^{39}Ar$ ages on a single H*P*-L*T* phengite grain distributed between 36.5 ± 0.4 and 30.8 ± 0.4 Ma (mean age = 35.1 ± 0.4 Ma) and interpreted to date crystallization during top-to-the-SW shearing in H*P*-L*T* conditions (see Figure 1; Brunet et al., 2000). Phengite step-heating analyses also yield older ages up to 47 Ma with internally discordant spectra potentially reflecting mixing between different reservoirs possibly including extraneous Ar. Younger, more concordant $^{40}Ar/^{39}Ar$ spectra near ~25 Ma were also obtained on highly strained rocks associated with the retrogressive top-to-the-NE motion along the ETSZ and considered as the final increments of deformation (see Figure 1; Brunet et al., 2000). A Rb-Sr study on phengite (see Figure 1; Rossetti et al., 2015) provided ages of 30.8 ± 4.2, 31.8 ± 1.7,

31.5 ± 2.5 Ma (top-to-the-SW shear zone), 27.1 ± 0.3 Ma (top-to-the-SW shear zone partially overprinted by semi-brittle top-to-the-NE shearing; not considered further in the text), and 20.2 ± 2.2 Ma (top-to-the-NE shear zone in its most deformed domains). This temporal sequence is considered as recording the end of the two shearing events. Final exhumation stages are recorded by zircon and apatite fission track data (ZFT and AFT). ZFT ages between 25 and 17 Ma in the Tenda massif and the Schistes Lustrés nappe are interpreted to date cooling with no significant age difference from either sides of the ETSZ (Fellin et al., 2006). AFT ages between 25 and 10 Ma (Cavazza et al., 2001; Danisik et al., 2007; Zarki-Jakni et al., 2004) are comparable between the different units, indicating no differential cooling between units during Miocene denudation.

The recent $^{40}Ar/^{39}Ar$ study of Di Vincenzo et al. (2016) has provided ages of 45–32 Ma in the Variscan basement of central Corsica, interpreted to constrain syn-burial crystallization of phengite near 35 Ma, and syn-exhumation re-equilibration after 33 Ma at a depth of ~18 km. These ages raise again the question of the timing of *HP-LT* metamorphism in the external domains, diversely interpreted as post- or pre-Priabonian (38–34 Ma) by stratigraphic data.

3. Sampling Strategy

The sampling strategy is based on the recent work of Beaudoin et al. (2017) where strain gradients were mapped. They defined six strain grades encompassing the different deformation events described above and locally overlapping as a result of spatial-temporal variations in strain distribution. As the S_2/L_2 and top-to-the-NE shear bands are considered as the main rocks fabrics in the ETSZ in their model, the strain grades are defined relative to D_2 and are based on structural relationships and mineral deformation/recrystallization textures between overlapping fabrics. This model, together with the other two structural/rheological models presented in section 2.2, will be discussed in the light of the new age data. Strain grades are summarized below:

Grade 0s.s.: undeformed to slightly deformed rocks (white mica crystallization only incipient; no $^{40}Ar/^{39}Ar$ sampling),

Grade 0W: D_1 deformation with S_1, L_1 and top-to-the-SW shear bands (C_1 shear bands).

Grade 1: D_2 deformation with folded S_1 between S_2 crenulation cleavage, associated with L_2 with a large amount of pure shear component,

Grade 2: local top-to-the-NE shear bands (C_2 shear bands) in an otherwise crenulation-dominated fabric (no $^{40}Ar/^{39}Ar$ sampling),

Grade 3: top-to-the-NE mylonitic fabric completely transposing S_1 with local preservation of D_2 folds,

Grade 4: higher-strain top-to-the-NE mylonites displaying more tightly spaced (<1 cm), low-angle shear bands (<30° to S_2) relative to Grade 3.

The strain grade map interpolated in Beaudoin et al. (2017) is reproduced in Figure 2 to show the regional strain pattern and gradients. Note that strain gradients are heterogeneous such that rocks from different strain grades can be locally encountered in a single strain grade zone.

From the initial sampling, 11 samples visually devoid of any sign of fluid circulation/weathering were selected to avoid secondary complications unrelated to deformation. These are mostly located along the main road and the sea shore where the rocks are the freshest. The distribution of the selected samples (Figure 2; Table 1) encompasses localized shear zones and associated strain gradients (outcrop and hand-sample scales) throughout the ETSZ while ensuring sufficient regional coverage to allow correlation of deformation-age relationships across the ETSZ. Table 1 provides the correspondence between strain grades and sample numbering. Because it is the most prevalently exposed fabric, sampling was mainly concentrated across D_2 strain gradients, except sample TE84, sampled within a D_1 top-to-the-SW shear zone (with three zones I, II, and III, from core to border) previously studied by Maggi et al. (2012). Sampling was focused on the compositionally homogeneous Mt. Asto monzogranite protolith, except for two meta-aplites (TE09 and TE41), a meta-basite (TE84-zone I), and a meta-rhyolite (TE52), this last from the Saleccia shear zone. Microstructural characteristics and chemical composition of white mica aggregates

Tectonics

10.1029/2020TC006246

Table 1
Synthesis of Structural and Petrological Characteristics of Samples

Sample	Strain grade	Domains	Protolith	Mineral assemblage	Structures	Microstuctures	Min-max grain size	Average grain size	Chemical heterogeneity (X-ray map composition)
TE61	0W	—	Granite	Qz + Ab + WM + mag. Kfs + (Ap + Mnz + Zr + Ep)	S_1 layers	Rare micro shear bands	10–400 μm	Coarse	Core (Al-rich) and rim (Fe (Mg)-rich) zonation
TE84*	0W	Zone III: out of SZ	Granite	Qz + Ab + WM + mag. Kfs + (Ap + Mnz + Zr + Ep)	S_1 layers	Rare micro shear bands	10–350 μm	Coarse	Core (Al-Fe-rich) and rim (Si-Mg-rich) zonation
		Zone II: border of SZ	Granite	Qz + Ab + WM + (Ap + Mnz + Zr + Ep)	S_1 layers	Rare micro shear bands	10–350 μm	Coarse	Core (Al-Fe-rich) and rim (Mg-rich) zonation
		Zone I: core of SZ	Basite	WM + Cpx + (Ap + Mnz + Zr + Ep + Qz + Chl)	—	C_1/S_1 structures	10–50 μm	Fine	Homogeneous
TE38	1	—	Granite	Qz + Ab + WM + (Ap + Mnz + Zr + Ep + Chl)	Folded S_1; S_2	Micro-folded S_1; S_2	10–400 μm	Medium	Homogeneous
TE47	1	—	Granite	Qz + Ab + WM + (Ap + Mnz + Zr + Kfs)	Folded S_1; S_2	Micro-folded S_1; S_2	10–300 μm	Medium	Homogeneous
TE62*	1	_	Granite	Qz + Ab + WM + (Ap + Mnz + Zr + Ep + Chl)	Folded S_1; S_2	Micro-folded S_1; S_2	10–200 μm	Fine	Al-rich and K-Fe-poor S2 compared to S1
TE43	3	Crenulated zone	Granite	Qz + Ab + WM + (Ap + Mnz + Zr + Ep)	Folded S_1; S_2	Micro-folded S_1; S_2	10–300 μm	Medium	Homogeneous
		Sheared zone	Granite	Qz + Ab + WM + (Ap + Mnz + Zr + Ep)	C_2 or S_2 layers	Transposed grains and relical S_1	10–300 μm	Medium	Homogeneous
TE52	4	_	Rhyolite	Qz + Ab + WM + Ep + (Ap + Mnz + Zr + Kfs)	C_2 or S_2 layers	Transposed grains and relical S_1	10–175 μm	Medium	Patchy zonation; Al-rich and Fe-rich zones
TE77*	4	_	Granite	Qz + Ab + WM + Ep + (Ap + Mnz + Zr + Kfs)	C_2 or S_2 layers	Transposed grains and relical S_1	10–350 μm	Coarse	Homogeneous
TE86	4	_	Granite	Qz + Ab + WM + (Ap + Mnz + Zr + Ep)	C_2 or S_2 layers	Transposed grains and relical S_1	10–400 μm	Coarse	Patchy zonation; Al-rich and Fe-rich zones
TE09	4	_	Aplite	Qz + Ab + WM + (Ap + Mnz + Zr + Ep)	Thin C_2 layers	Total transposition of grains	10–300 μm	Medium	Homogeneous
TE41	4	_	Aplite	Qz + Ab + WM + (Ap + Mnz + Zr + Ep + Chl)	Thin C_2 layers	Total transposition of grains	10–300 μm	Coarse	Patchy zonation; Al-rich and Fe-rich zones Variations in K content

Note. Grain size is characterized by the minimal and maximal apparent diameter of crystal flakes along with the average grain size parallel to the (001) cleavage in white mica aggregates. "Coarse" designates grain size greater than ~150 μm, "medium" between 100 and 150 μm, and "fine" smaller than 100 μm and are average grain sizes. Grain size were checked on transversal planes from XZ thin section. It was also checked on XY thin sections for eight samples in order the get true diameters on basal planes. Since structures are undulated, those thin sections display only few basal sections, that globally give the same diameter as XZ sections, as the apparent aspect ratio on basal plane is near 1:1.

were checked for all dated samples. Structural formula derived from microprobe analysis were calculated with a minimum of ~50 punctual analyses per sample in order to have a statistically representative estimate of the compositional homogeneity of aggregates. Furthermore, compositional maps were acquired in order to image spatial variations in chemical composition across aggregates potentially containing several mineral generations.

4. Analytical Procedure

Petrographical observations were carried out on polished sections with an optical microscope and a back-scattered electron imaging detector (BSE) from a Merlin Compact ZEISS scanning electron microscope (SEM) operating at 15 kV (ISTO, University of Orléans, France). Compositional maps were acquired with an associated X-ray energy dispersive system (EDS). Electron microprobe analyses (EMPA) were carried out using a CAMECA SX Five electron microprobe equipped with five wavelength-dispersive spectrometers operating at 15 kV and a current of 6 nA (ISTO).

For in situ $^{40}Ar/^{39}Ar$ dating, rock sections of 1 cm diameter were drilled from XZ hand-sample sections, then polished and metallized for imaging. Sections were then re-polished and washed ultrasonically through three successive ultrasonic baths (acetone, ethanol, and pure water), each one followed by drying in a 50°C stove. No glue was used through the entire protocol. For step-heating $^{40}Ar/^{39}Ar$ dating, small-sized (<2 mm) cohesive white mica aggregates were picked up from XZ hand-sample sections. Unlike standard concentrates homogenized over several cm^3, these provide a bulk (population-like) age with mm-scale textural control (Figure 4). After very careful inspection under a binocular microscope to remove any adhering phase/contaminant, these were cleaned through three successive ultrasonic baths (acetone, ethanol, and pure water), each one followed by drying in a 50°C stove, before final optical inspection and weighing.

For irradiation, in situ sections were stacked in a customized Al can with 1.5 mm thick Al disk holders in between each sample and loaded with Fish Canyon sanidine as the irradiation monitor (FCS = 28.02 ± 0.28 Ma; Renne et al., 1998). Each monitor holder contains up to 13 loading positions (one in the center and six distributed radially in two concentric circles) to provide 3D neutron flux control. Alignment between polished sections and standard levels was checked before and after irradiation. Aggregates used for the bulkwise step-heating approach were individually wrapped in Al foils and stacked in a dedicated, 5 mm OD diameter, Al can with monitor packets (each loaded with two Fish Canyon sanidine grains) interspersed every four samples. Simultaneous irradiation of both cans lasted for 5 hr in the Cd-lined CLICIT port of the OSU reactor facility (Corvalis, USA).

In situ analyses were performed with a LSX 213-G2 UV deep-UV CETAC® (213 nm) pulsed laser operating at 20 Hz and 3.5 mJ/pulse. A minimum spot size of 50 μm (max. 100 μm) was applied to ensure a favorable sample/blank ratio while allowing spatially resolved inter-grain targeting (mean crystal size was ~50–100 μm, precluding intra-grain variations to be resolved). Step-heating analyses were conducted with a continuous-wave 25 W Synrad® CO_2 laser (Scaillet et al., 2013) defocused to twice as much as the size of the sample lying on a stainless steel holder underneath a differentially pumped ZnS viewport, each step consisting in 30 s exposure to the beam (at sequentially higher laser-power steps until complete melting).

The extracted gas was purified for 6 min using a cold trap held at −127°C, two air-cooled GP50 SAES® getters at 250°C, and two hot Ta filaments held at 1,500°C, before admission into one of the three static noble gas Helix-SFT Thermo Scientific® mass-spectrometers operated at ISTO with a mass resolution in excess of 750. Ar and Cl isotopes were sequentially measured in 20 cycles with an electron multiplier (^{35}Cl, $^{36}Ar \pm {}^{1}H^{35}Cl$, $^{37}Ar \pm {}^{37}Cl$, $^{38}Ar \pm {}^{1}H^{37}Cl$, ^{39}Ar, ^{40}Ar isotopes) and a Faraday cup (^{40}Ar only) by peak-switching. Gas handling and mass-spectrometer operations are fully automated using in-house, stand-alone LabView-based software interfacing gas extraction and data collection. Procedural blanks were analyzed every sample gas admission (in situ experiments) or every third heating step (step-heating experiments) in the same conditions as the sample analysis. Typical values were 0.1–0.05 fA and ~0.001 fA for m/e = 40 and m/e = 39, 38, 37, 36, respectively. Data regression and age calculations/corrections were made following Scaillet (2000). Regressed $^{40}Ar/^{39}Ar$ isotopic data are tabulated either as $^{40}Ar/^{39}Ar$ step-heating analyses and in situ $^{40}Ar/^{39}Ar$ analyses in the supporting information. Individual age errors include propagation of all instrumental and procedural uncertainties. Total sample (bulk) ages are reported as integrated

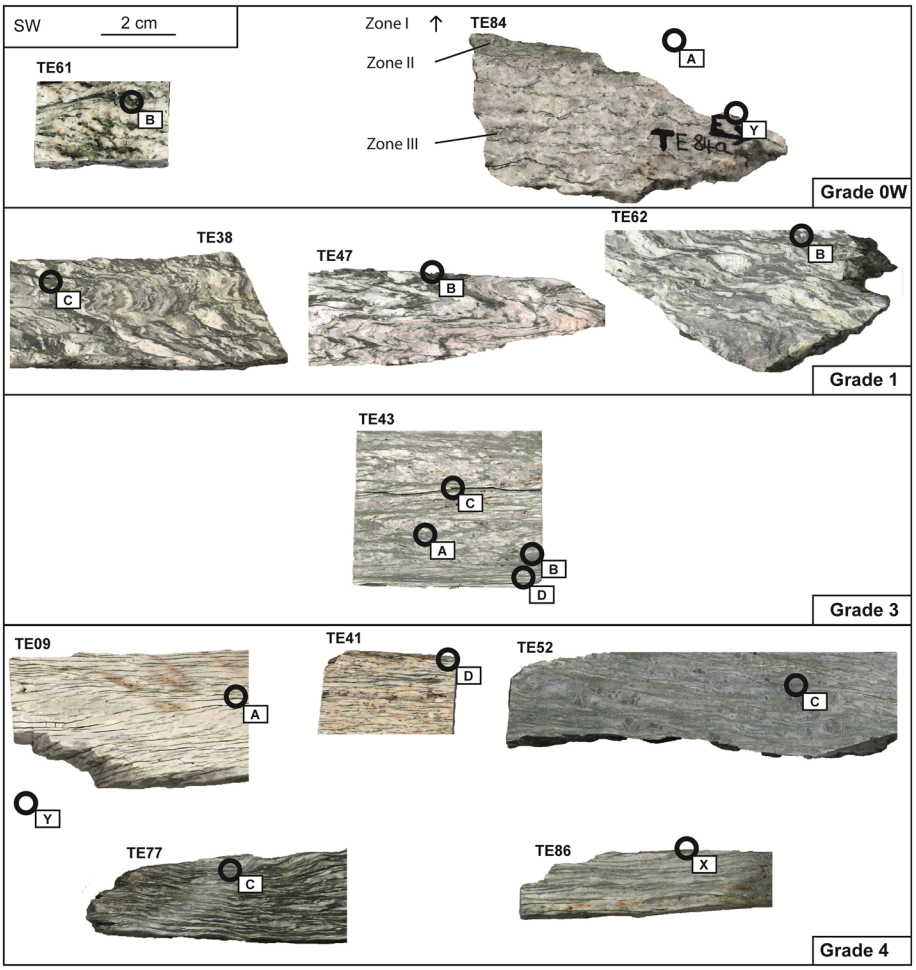

Figure 4. Pictures of samples and in situ location of white mica population sampled for step-heating experiments. Each analyzed aggregate is identified by a bold letter. The scale and the orientation is the same for all pictures. Some dated aggregates were not sampled directly from the rock sections as displayed but a few mm apart (as indicated by the symbol outside the section limits).

(inverse-variance weighted mean) and total-gas (individually summing the Ar isotopes of all steps) ages quoted at $\pm 1\sigma$.

5. Microstructural Analysis

In all samples, the main metamorphic fabric is composed of alternating greenish mica-layers and quartz + feldspar layers (magmatic K-feldspar relics and ubiquitous metamorphic albite) ± chlorite, accessory epidote, Fe-Ti oxides, apatite, monazite, and zircon. Metabasite TE84-zone I stands apart with white mica (>80%) and clinopyroxene as main minerals. Sample characteristics, including strain grade, structural domains, type of protolith, mineralogical assemblage, structures, microstructures, grain size with maximum/minimum length along basal section (001), and average referred as fine (<100 μm), medium (100–150 μm), and coarse (>150 μm) and chemical zoning are listed in Table 1.

5.1. Grade 0W

Meta-granite TE61 is characterized by S_1 and C_1 shear bands localized either in white mica or quartz-feldspar aggregates (Figure 4). Microscopically, S_1 is lined by white mica aggregates (Figure 5a). Crystals are on average coarse-grained, even if fine-grained zones exist. They show evidence of intracrystalline deformation such as undulose extinction and gentle (001) bending with grain segmentation linked to viscous/brittle behavior (Figures 5b and 5c). Large grains can be segmented via kink-bands or cracks

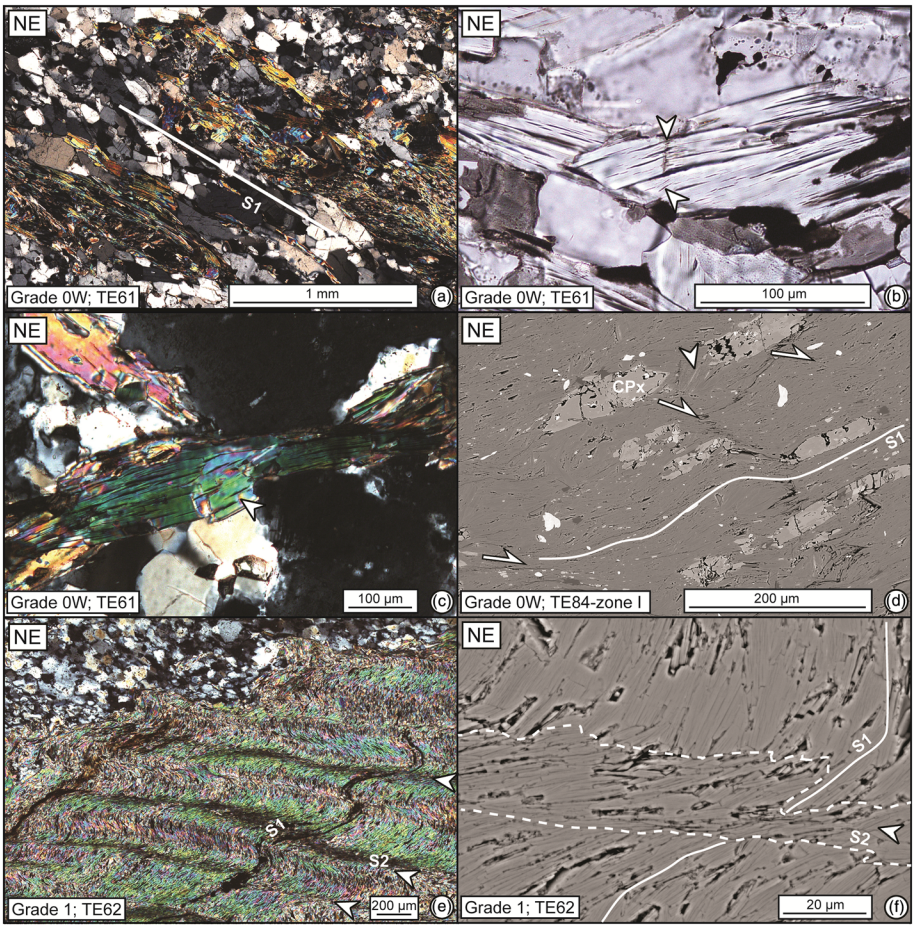

Figure 5a. Microstructural observations of white mica aggregates. Strain grade is indicated for each pictures. (a) Lattice preferred orientation with (001) parallel to S_1 in Grade 0W. (b) Bending and kinking of (001) associated (top arrow) or not (bottom arrow) with cracking normal to (001). (c) Grain segmentation. (d) C_1/S_1 structures in clinopyroxene/white mica aggregate in TE84-zone I. (e) Folded S_1 between S_2 cleavage (arrows) in Grade 1. (f) Recrystallized grains in S_2. Note that folding in S_1 is achieved through different strain free grains that are progressively misoriented from each other. (g, h) Transposition of grains in C_2 shear zones in Grade 3. (i, j) Coarse grains aligned in C_2 shear bands between microlithons domains with oblique grains (white arrow) in Grade 4. (k, l) Almost total transposition of grains in discrete layers in meta-aplites of Grade 4.

sub-normal to (001), that sometimes appear serrated, separating slightly misoriented domains, resulting in the reduction of the average grain size (Figures 5b and 5c).

Meta-basite TE84 is composed of three different zones (Figure 4). Zone I (core of shear zone) is characterized by regular C_1/S_1 structures in white mica-clinopyroxene aggregates (Figure 5d). Grains are totally transposed into S_1 with an average grain size smaller than 50 µm and show rare evidence of chlorite precipitation along cleavage or along boundaries (see white arrow; Figure 5d). Zone III (outside the shear zone) displays structures comparable to sample TE61 described above. Zone II is located in between and resembles zone III except that it is characterized by a higher content of white mica and the lack of relic K-feldspar. Incipient crenulation is seen to affect the D_1 fabric as a result of D_2 reworking (see Figure 8 for the outcrop description).

5.2. Grade 1

Grade 1 (meta-granites TE38, TE47, and TE62) is characterized by folded S_1 microlithons between S_2 crenulation cleavage (Figures 4 and 5e). S_2 fabric is planar and defined either by a sharp change in S_1 orientation or by crystallization of new white mica crystals (Figure 5f). Rare evidence of chlorite precipitation along

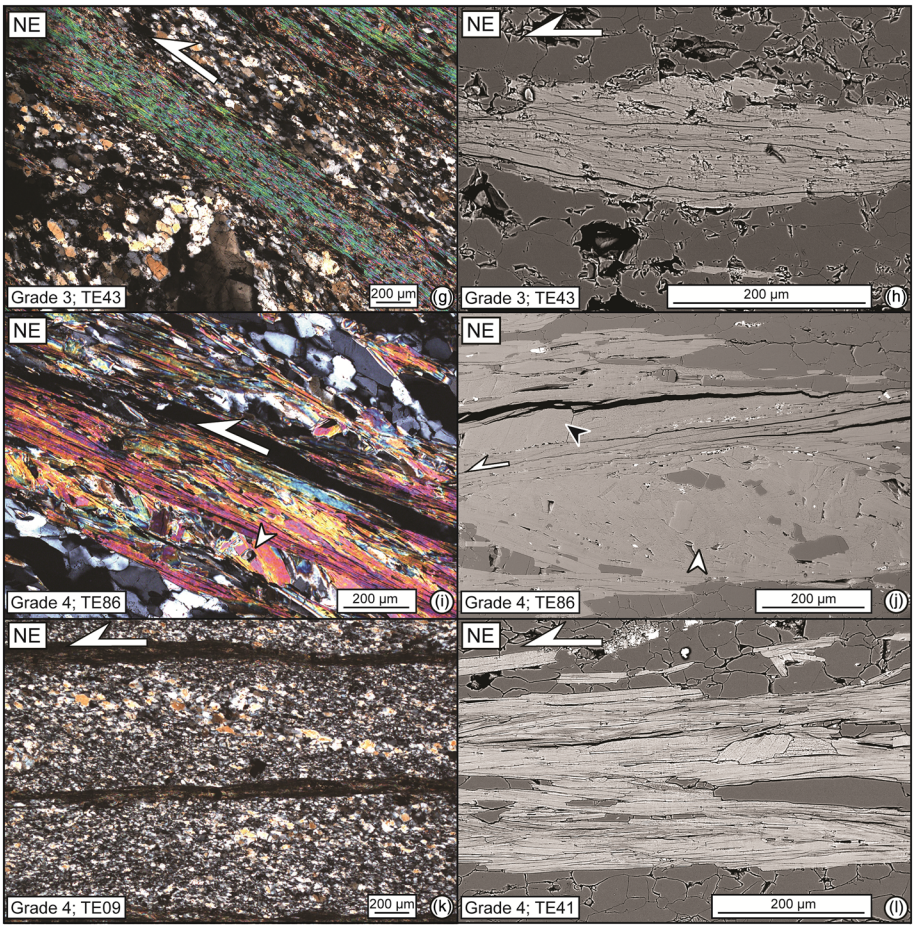

Figure 5b. (continued)

cleavage or grain boundaries is found in TE38 and TE62. Bending of S_1 into S_2 reflects internal deformation (undulose extinction) but is revealed by SEM examination to involve small grains progressively misoriented from each other with no apparent internal deformation. White mica is fine- to medium-grained and grain size is on average smaller and thinner than in Grade 0W for the same protolith (TE61). Grains marking the S_2 are smaller than the grains forming S_1 (Figure 5f).

5.3. Grade 3

Grade 3 (meta-granite TE43) is mostly characterized by low-strained zones that preserve crenulation structures between sheared zones displaying C_2/S_2 structures (Figure 4). Crenulated zones have the same microstructural characteristics as Grade 1. In more deformed zones, C_2 shear bands lie at shallow angle to S_2 (<10°; Figure 4), rendering their recognition difficult (Figures 5g and 5h). Here, the grain size of white mica is comparable to previous strain grades but crystals appear almost totally transposed.

5.4. Grade 4

The meta-granites (TE77, TE86) and meta-rhyolite (TE52) are characterized by homogeneous C_2/S_2 structures (Figure 4). Microscopically, white mica aggregates are either transposed in C_2 shear bands or define sigmoidal microlithons in between (Figures 5i and 5j). Grains within shear bands have a coarser grain size (until >400 µm) but a thinner thickness than in microlithons (Figures 5i and 5j). Grains oriented perpendicular to shear bands can be fractured (Figure 5j).

Meta-aplites (TE09 and TE41) are characterized macroscopically (Figure 4) and microscopically (Figures 5k and 5l) by concordant white mica and quartz-feldspar layers lacking clear shearing sense due to decreasing angle between C_2 and S_2. White mica grains are totally transposed in the aggregates (Figure 5l).

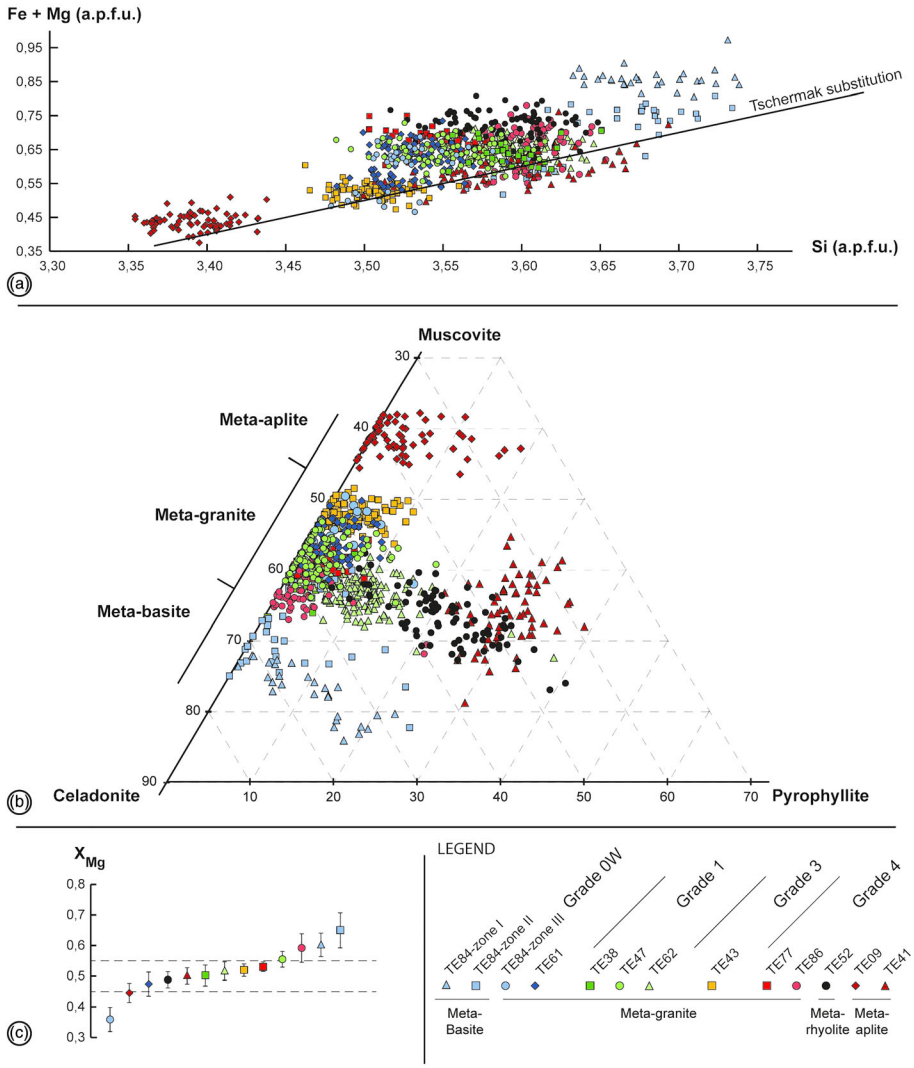

Figure 6. Chemical composition of white mica. Data are differentiated by colors and marker shapes, indicating both samples and strain grade (see legend). (a) Fe + Mg versus Si plot. Data are broadly aligned along the Tschermak substitution but are clustered by sample, reflecting bulk-rock compositional control. Data plotting off the Tschermak substitution line indicate the existence of other components (substitutions). (b) Muscovite-celadonite-pyrophyllite ternary diagram showing a pyrophyllite substitution, in particular for samples TE41 and TE52 where the pyrophyllite component reaches 20–40%. (c) Average X_{Mg} of phengite. Brackets represent standard deviation.

Average grain size in Grade 4 is similar to the other strain grades, showing that neither systematic nor consistent grain size reduction accompanied the increase in deformation intensity.

6. White Mica Composition

Compositional data show that white micas are phengites that broadly plot along the Tschermak substitution line in the Fe + Mg versus Si plot (Figure 6a). They show highly variable celadonite content, with Si and Fe + Mg ranging between 3.35–3.75 and 0.35–0.95 a.p.f.u., respectively. Analyses are clustered independent from strain grade, but primarily as function of lithology (bulk-rock control). Phengites with the lowest celadonite content (i.e., Si = 3.35–3.45 a.p.f.u.) belong to the relatively Fe-Mg poor meta-aplite TE09, while phengites with the highest celadonite content (i.e., Si = 3.65–3.75 a.p.f.u.) belong to the Fe-Mg rich meta-basite TE84-zone I. All remaining granite-derived samples plot between 3.45 and 3.65 a.p.f.u. On average, the data slightly plot off the ideal Tschermak substitution line (Figure 6a) with an amount of pyrophyllite component between 0% and 15% (Figure 6b) revealed by K contents comprised between 0.70 and 1.05 a.p.f.u. (see table

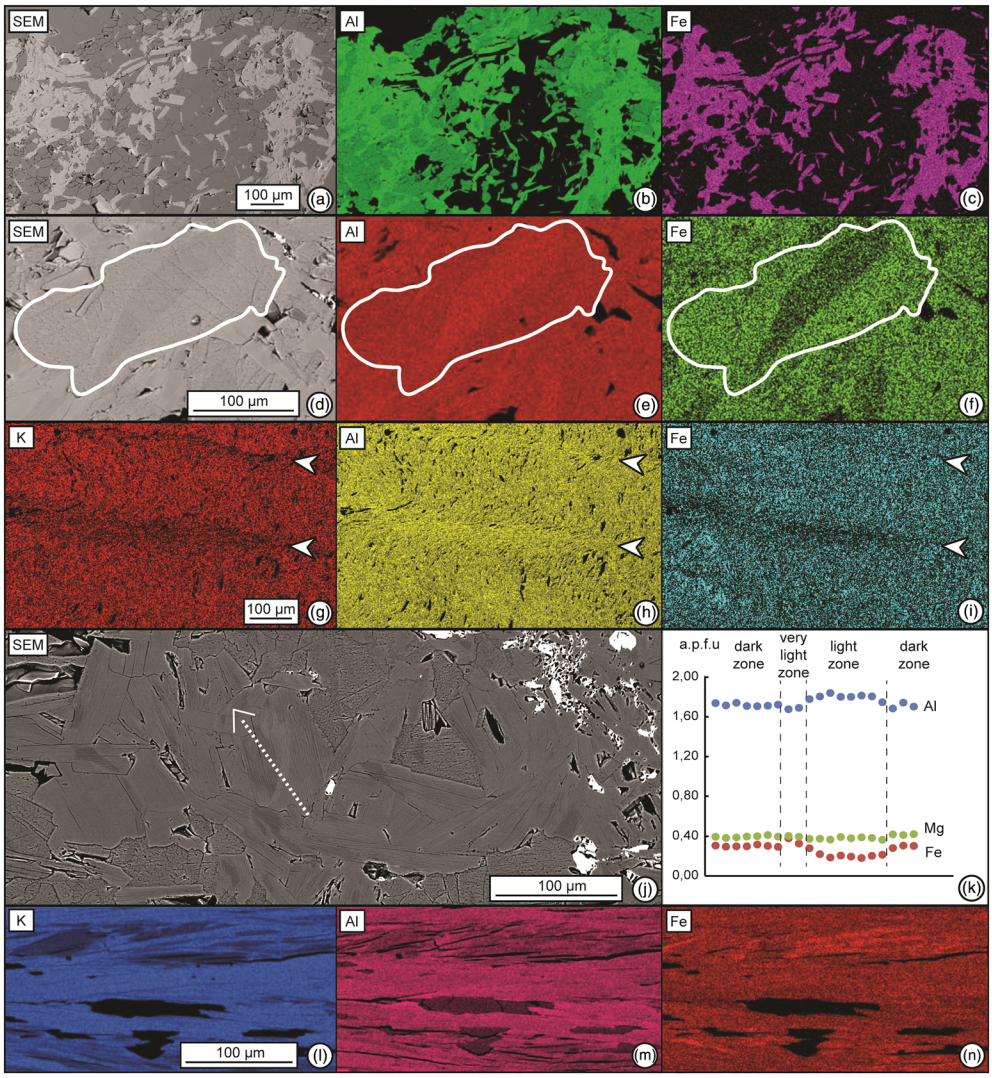

Figure 7. SEM and XRD compositional maps in phengite aggregates. (a, b, c) illustrate homogeneous Al and Fe concentration in some samples (XY sections). (d, e, f) Core (Al-rich)-rim (Fe-rich) zoning in a grain from Grade 0W. (g, h, i) Relative enrichment in Al and depletion in K and Fe in S_2-phengite (arrows) compared to S_1-phengite in Grade 1. (j, k) Al, Mg, and Fe zoning that is not associated with core-rim textures anymore (XY section). (l) Heterogeneous distribution of K interfering with other zonations involving Al (m) and Fe (n) in samples with pyrophyllite-rich phengite.

"chemical composition of white mica" in the supporting information). Two samples show a distinctly higher pyrophyllite component, between 10% and 40% (meta-rhyolite TE52) and between 20% and 35% (meta-aplite TE41). The X_{Mg} is comprised between 0.45 and 0.55 in most samples, but four are out of this range (Figure 6c). Zone III of meta-basite TE84 contains phengites with relatively low mean X_{Mg} at 0.36 ± 0.04, while zones I and II display relatively high mean X_{Mg} at 0.65 ± 0.06 and 0.60 ± 0.04, respectively. Meta-granite TE86 also has a high mean X_{Mg} at 0.59 ± 0.05.

X-ray compositional maps show different types of chemical zoning in Fe, Al, and K (Figure 7), listed in Table 1 for all samples. Half of the samples are devoid of significant chemical zoning (Figures 7a–7c and Table 1). Other samples show variable zoning patterns marked by anti-correlated Al-rich (dark gray) zones and Fe-rich (light gray) zones in SEM pictures (Figure 7). Phengites from Grade 0W can show clear core-rim zonations (Figures 7d–7f and Table 1). A general trend can be seen between Al-rich cores and Fe- or Mg-rich (sometimes Si-rich) rims, with a possible decorrelation between Fe and Mg. Crenulated zones in Grades 1–3 display correlation between phengite composition and textural habitus with S_2-micas distinctly showing an

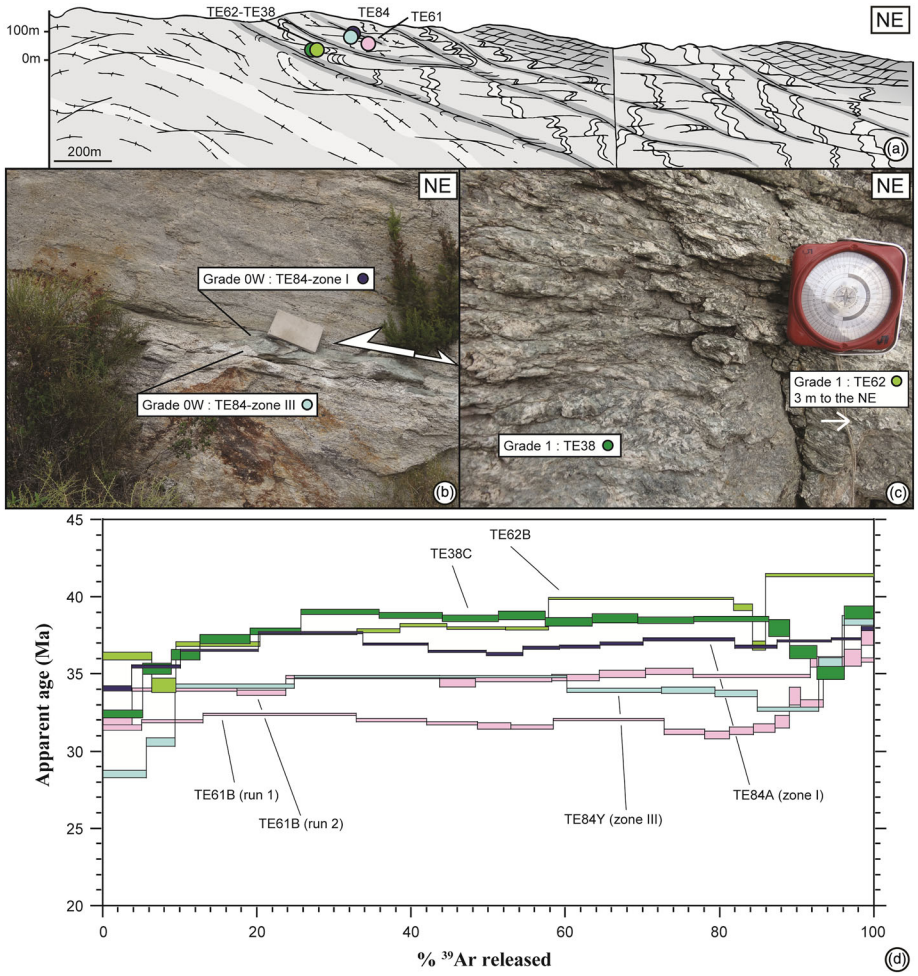

Figure 8. Step-heating analyses from Grades 0W and 1 from cross section 1 (see Figure 2). (a) Cross section showing deformation features and samples location. (b) Outcrop picture of sample TE84 (Grade 0W). Top-to-the-NE indicators show a weak reworking of this thick shear band localized in a meta-basite, but the thin section shows pervasive top-to-the-SW shear bands (see Figure 5d). (c) Outcrop picture of sample TE38 (Grade 1) showing crenulated structures. (d) Step-heating spectra.

apparent depletion in K and Fe and an enrichment in Al (Figures 7–7i and Table 1). Chemical zoning of phengite is not systematic in these samples (see Table 1). When present, it is irregular in the more strained ones (Grades 3–4) with no clear core-rim trend (Figure 7j). In these cases, it is systematically marked by Al-rich (dark gray) zones and Fe-rich (light gray) zones, such as in Grade 0W (Figures 7j and 7k). Samples displaying a marked pyrophyllite component show the same Al-Fe zoning along with an interfering K zoning, also irregular and not systematically correlated with other elements (Figures 7l–7n).

7. $^{40}Ar/^{39}Ar$ Results

Results are presented in tables "$^{40}Ar/^{39}Ar$ step-heating analyses" and "$^{40}Ar/^{39}Ar$ in situ analyses" in the supporting information along with $^{38}Ar/^{39}Ar$ (Cl/K) and $^{37}Ar/^{39}Ar$ (Ca/K) ratios not displayed in the figures. These were all close or within error of zero, indicating no significant contribution from Ca- or Cl-rich impurities or contaminating phases.

7.1. Step-Heating Data

$^{40}Ar/^{39}Ar$ age spectra are presented along three W-E to SW-NE cross sections over which structural position of the samples is projected, showing the transition from deep to shallower levels of the Tenda Massif toward the ETSZ (see Figure 2 for location). Reported synthetic cross sections display the structural-spatial

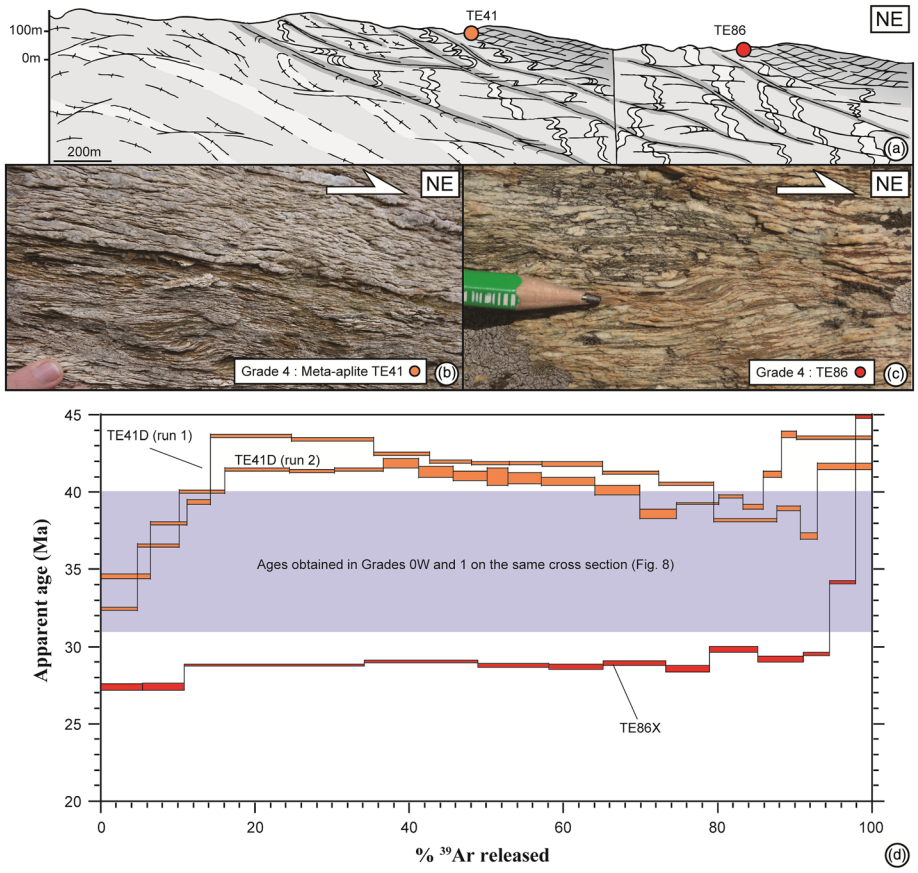

Figure 9. Step-heating analyses from Grade 4 from cross section 1 (see Figure 2). (a) Cross section showing deformation features and samples location. (b, c) Outcrop pictures of meta-aplite TE41 and meta-granite TE86 showing parallelization of S_2 and C_2 shear bands. Few top-to-the-NE indicators remain. (d) Step-heating spectra.

relationships along with outcrop pictures and a synthetic spectrum plot collecting the relevant step-heating results. The same color code is used to identify samples across the different displays.

7.1.1. Cross Section 1: Southern Area

This cross section, along the main road to Saint-Florent, cuts across the entire strain grade evolution (Figure 8a), from Grade 0W (lower parts and low-strain domains), through Grade 1 (middle parts), and Grade 4 (topmost parts). Data are presented in two figures, one for the (western) basal parts of the cross section (Grades 0W and 1; Figure 8) and one for the (eastern) top parts (Grade 4; Figure 9).

Grade 0W was not sampled in the lowest part of the section due to extensive weathering but was selected into low-strain boudins within Grade 1 zone (Figure 8a). Two are from the same outcrop, in the core (meta-basite) and the border (meta-granite) of the top-to-the-SW shear zone partially overprinted during D_2 (zones I and III from sample TE84, respectively; Figure 8b). The third lies about 50 m further east (TE61; meta-granite) and resembles TE84-zone III in terms of structures. Phengites from TE84-zone I (TE84A; Figures 4 and 8d) yielded an oscillating spectrum between 34 and 38 Ma. The total gas age is 36.8 ± 0.2 Ma. Phengites from TE84-zone III (TE84Y; Figures 4 and 8d) also yielded an oscillating spectrum between 28 and 38 Ma with a younger total gas age of 33.9 ± 0.2 Ma. Phengites from TE61, sampled along S_1 (TE61B; Figure 4) were analyzed twice (Figure 8d). The first run yielded a relatively concordant spectrum with a nearly flat segment between 31 and 32 Ma over 90% of the total ^{39}Ar released, followed by increasing ages climbing to ~36 Ma with a total gas age of 32.2 ± 0.1 Ma. The second run yielded a similar shape with older ages and a nearly flat segment between 34 and 35 Ma over 92% of the total ^{39}Ar released, followed by an increase to ~37 Ma until the end of the spectrum. The total gas age is 34.6 ± 0.2 Ma.

Two meta-granites from Grade 1, TE38 and TE62, were collected 3 m apart in the same outcrop (Figure 8c). Phengites from TE38, sampled in folded S_1 (TE38C; Figures 4 and 8d) yielded an upward convex spectrum with minimum apparent age at ~32 and 35 Ma, respectively, at the beginning and the end of the analysis, and a maximum with a nearly flat segment at ~39 Ma between 25% and 85% of the total ^{39}Ar released. The total gas age is 37.8 ± 0.2 Ma. Phengites from TE62 sampled in folded S_1 (TE62B; Figures 4 and 8d) also yielded an upward convex age spectrum with minimum apparent ages at ~34 and 37 Ma, respectively, at the beginning and the end of the analysis, with a maximum apparent age at ~40 Ma between 58% and 82% of the total ^{39}Ar released. The total gas age is 38.6 ± 0.2 Ma.

Toward the northeast, deformation evolves to Grade 4 (Figure 9a). Two samples were selected (meta-aplite TE41 and meta-granite TE86), separated by ~1 km from each other by a late sinistral brittle fault (see Figures 2 and 9a).

TE41 is an aplite-derived ultramylonite (Figure 9b). Phengites sampled along C_2 planes (TE41D; Figure 4) were analyzed twice (Figure 9d). The first run yielded an asymmetric upward convex age spectrum with a minimum apparent age at ~34 Ma at the beginning, increasing after to a maximum age of ~44 Ma between 15% and 35% of ^{39}Ar release, then falling back to ~36 Ma at the end. The total gas age is 40.8 ± 0.2 Ma. The second run has a similar shape but rising to ages about 2 Myr younger. The total gas age is nearly the same at 40.3 ± 0.2 Ma. These ages are significantly older than those from samples from the less deformed parts of the same section (indicated by the blue shaded domain in Figure 9d).

TE86 is a highly deformed meta-granite mylonite (Figure 9c). Phengites sampled in C_2 shear band or transposed S_2 (TE86X; Figures 4 and 9d) yielded a relatively concordant age spectrum with a nearly flat segment between ~28 and 30 Ma over the first 95% of the total ^{39}Ar released. The total gas age is 29.3 ± 0.1 Ma, younger than Grade 0W and Grade 1 samples of the same cross section (blue shaded area in Figure 9d).

7.1.2. Cross Section 2: Punta di Cepo

This cross section (Figure 10a) cuts across a large-scale strain gradient including the bottom (meta-granite TE47, Grade 1) and the top of the ETSZ (meta-granite TE43, Grade 3).

TE47 is characterized by recumbent microfolds of S_1 with a larger amplitude (up to 3 cm) than other Grade 1 samples (generally <1 cm), resulting in the obliteration of the top-to-the-SW shearing criteria (Figure 10b). Phengites sampled in folded S_1 (TE47B; Figure 10b) yielded a ^{40}Ar loss-like spectrum between ~31 and 36 Ma from 3% to 24% of the total ^{39}Ar released, followed by a flat segment at ~36 Ma until 98% of the total ^{39}Ar released (Figure 10d). The total gas age is 35.3 ± 0.2 Ma.

TE43 is characterized by crenulated domains traversed by top-to-the-NE shear zones (Figure 10c). Four phengite aggregates were sampled, two in crenulated domains (TE43A and TE43B) and two in shear zones (TE43B and TE43C). They all provide ages on average 8 Myr younger than aggregate TE47B (Figure 10d). TE43A was analyzed twice. The first run yielded a ^{40}Ar loss-like spectrum starting at ~26 Ma and stabilizing around ~27–28 Ma between 10% and 96% of the ^{39}Ar released. The total gas age is 27.8 ± 0.1 Ma. The second run also yielded a ^{40}Ar loss-like spectrum starting at ~23 Ma stabilizing between ~26 and 27 between 20% and 98% of the ^{39}Ar released. The total gas age is 26.2 ± 0.2 Ma. TE43B yielded a relatively concordant age spectrum between 27 and 28 Ma from 12% to 94% of the total ^{39}Ar released. The total gas age is 27.6 ± 0.1 Ma. TE43C provided an upward convex age spectrum with minimum apparent age at ~25 and 23 Ma, and a maximum apparent age at ~28 Ma near 90% of the total ^{39}Ar. The total gas age is 26.9 ± 0.1 Ma. TE43D was analyzed twice. The first run yielded an upward convex age spectrum with minimum apparent age at ~24–24.5 Ma (<0% and >96% of total ^{39}Ar), and a maximum apparent age at ~25.5–26.0 Ma in between. The total gas age is 25.3 ± 0.1 Ma. The second run yielded a ^{40}Ar loss-like pattern between ~25 and 29 Ma. The total gas age is 26.7 ± 0.1 Ma.

7.1.3. Cross Section 3: Saleccia and Loto Beaches

This cross section (Figure 11a) exposes two main D_2 shear zones where strain is strongly localized, including the Saleccia shear zone (meta-rhyolite TE52; Figure 11b) and the ETSZ (meta-aplite ultramylonite TE09 and meta-granitic mylonite TE77, Figure 11c), the last providing a test on the possible influence of variable lithology in a single outcrop (Grade 4).

Phengites from meta-rhyolite TE52 (Saleccia shear zone) was sampled along S_2 (TE52C; Figure 4) and analyzed twice (Figure 11d). The first run yielded an age spectrum including a first flat segment at ~27.5 Ma

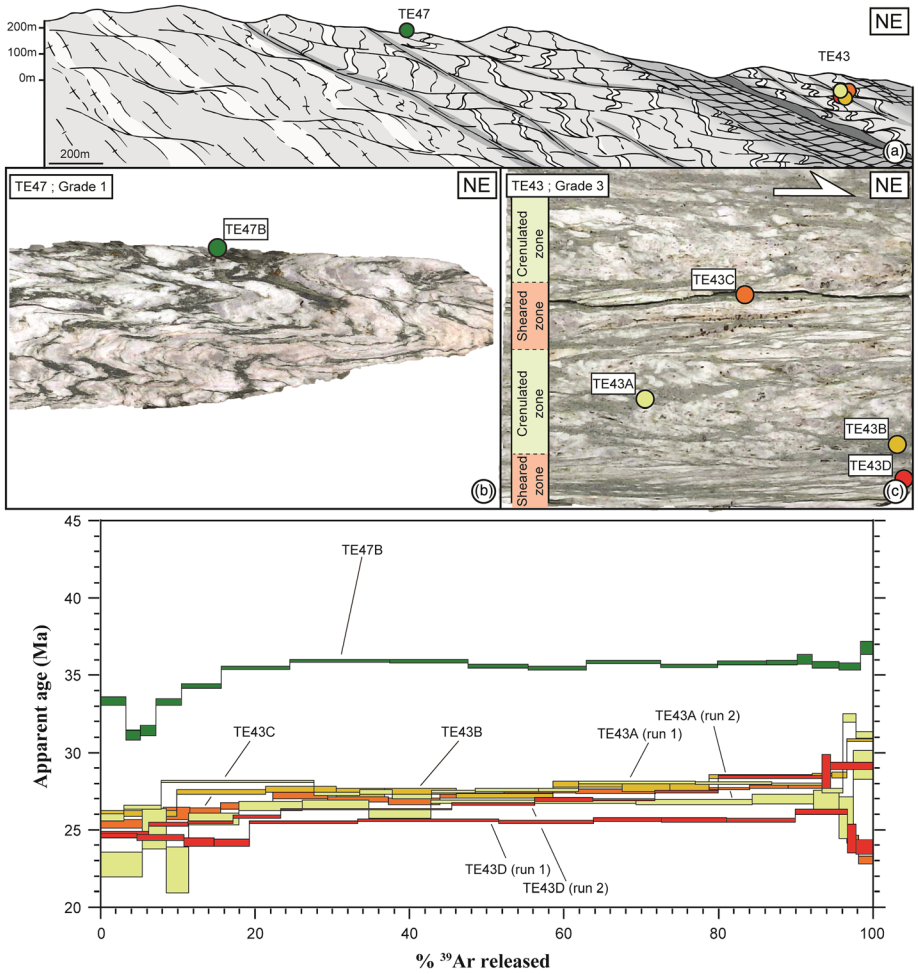

Figure 10. Step-heating analyses from cross section 2 (see Figure 2). (a) Cross section showing deformation features and samples location. (b) Hand-sample picture of sample TE47 (Grade 1) showing a strong crenulation structure. (c) Hand-sample picture of sample TE43 (Grade 3) showing crenulated structures preserved between highly sheared zones where C_2 shear bands and S_2 tend to parallelize. In situ location of analyzed aggregates are indicated. (d) Step-heating spectra.

followed by variable ages between ~28.5 and 29.5 Ma. The total gas age is 28.6 ± 0.1 Ma. The second run displays a ^{40}Ar loss-like pattern between ~27 and 30 Ma over the whole gas release. The total gas age is 28.2 ± 0.1 Ma.

Phengites from meta-granite TE77 (ETSZ), sampled along C_2 shear band or transposed S_2 (TE77C; Figure 4) were analyzed twice and globally yielded older ages than TE52C (Figure 11d). The first run yielded a ^{40}Ar loss-like pattern from ~28 to 31 Ma between 7% and 90% of the total ^{39}Ar released, the end of the spectrum being highly discordant between 34 and 39 Ma. The total gas age is 30.8 ± 0.1 Ma. The second run yielded a similar ^{40}Ar loss-like spectrum from ~26 to 31 Ma with a total gas age of 29.3 ± 0.1 Ma.

Two phengite aggregates from the meta-aplite TE09 (ETSZ), sampled along a C_2 plane (TE09A and TE09Y; Figure 4) provided younger ages than TE77C and TE52C (Figure 11d). The first one yielded a very discordant age spectrum with a ^{40}Ar loss-like profile from ~23 and 29 Ma with an overall complex shape. The total gas age is 25.7 ± 0.1 Ma. The second one was more concordant, yet with still a complex shape between 25 and 28 Ma. The total gas age is 26.8 ± 0.1 Ma.

7.2. In Situ Data

In situ ^{40}Ar/^{39}Ar dating was applied to statistically quantify ages versus microstructure relationships according to strain grade and investigate the relationships with the age variations revealed by the corresponding

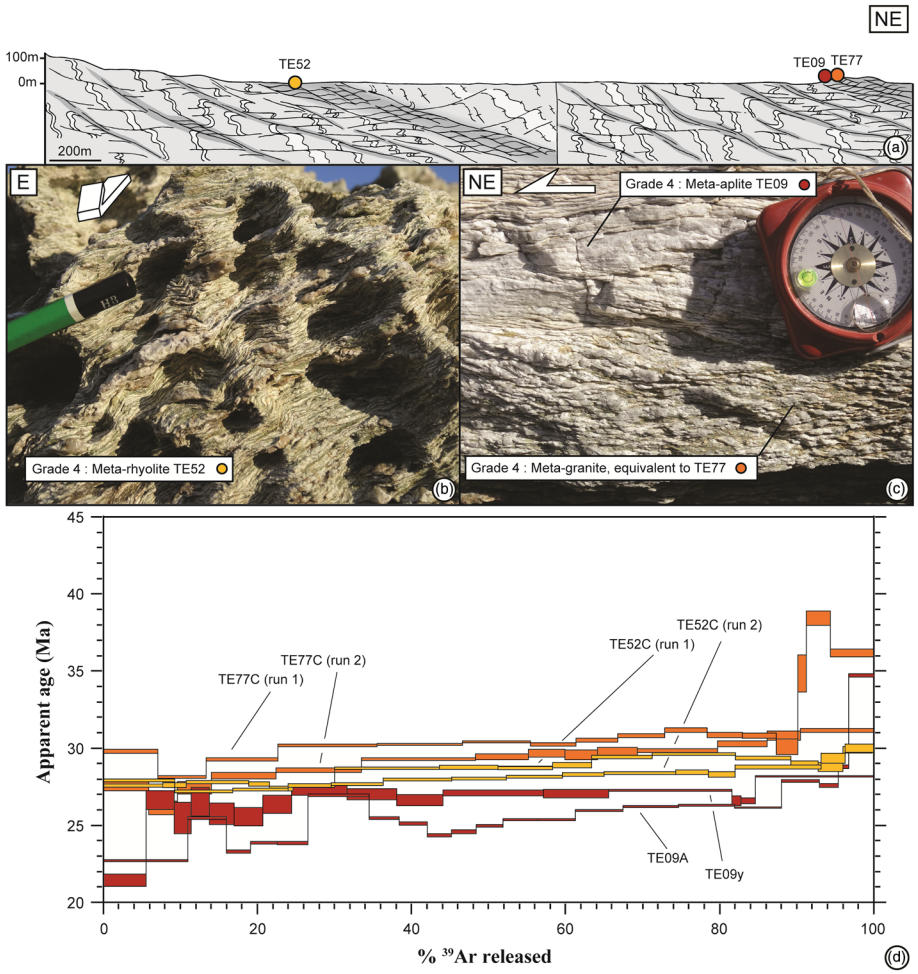

Figure 11. Step-heating analyses from cross section 3 (see Figure 2). (a) Cross section showing deformation features and samples location. (b) Outcrop picture of sample TE52 (Grade 4), deformed rhyolite from the Saleccia shear zone. (c) Outcrop picture of sample TE09 (ultramylonitic aplite) and an equivalent of sample TE77 (meta-granite mylonite; Grade 4), sampled few meters away, showing S_2/C_2 structures. (d) Step-heating spectra.

bulk $^{40}Ar/^{39}Ar$ step-heating data. Three polished sections from Grades 0W, 1, and 4 (TE84, TE62, TE77, respectively) were analyzed. Data are presented below either in the form of in situ age maps or sorted in situ ages spectra.

7.2.1. Grade 0W (Meta-Granite TE84)

Section TE84 (Figure 12) was drilled out across zones II and III in a top-to-the-SW localized shear zone (see Figure 8b). S_1 is marked by green phengite aggregates alternating with white quartz-feldspar layers (Figure 12a). Phengite is more abundant in zone II which lacks relic K-feldspar clasts as found in zone III. Sixty-eight analyses were gathered on phengite (43 in zone II, 25 in zone III) and 61 on K-feldspar (zone III). Phengite ages range between 27.2 ± 0.3 and 36.9 ± 2.9 Ma (Figure 12c). Statistically, older ages are prevalently found in zone II, hosting 84% of the ages older than 32 Ma, while zone III displays 89% of the ages younger than 32 Ma. The spatial age distribution is otherwise random in each sub-zone (Figure 12a). The first part of the spectrum of sorted ages, dominated by zone III ages, shows discordant ages between ~29 to 33 Ma between 2% and 34% of cumulative increase (Figure 12c). The remainder, mostly corresponding to zone II, is more concordant with a weak increase from ~33 to 35 Ma between 34% and 99% of cumulative increase. In situ ages in K-feldspar define a much broader, almost continuous, age range between 34.0 ± 0.5 and 141.9 ± 0.5 Ma. The spatial age distribution occurs without apparent microstructural control either between or within the clasts, but with older ages (>77 Ma) clearly associated with the larger crystals (Figure 12a). Noteworthy, the younger limit of K-feldspar age distribution nearly coincides with the oldest phengite component found at 35 Ma (Figure 12b).

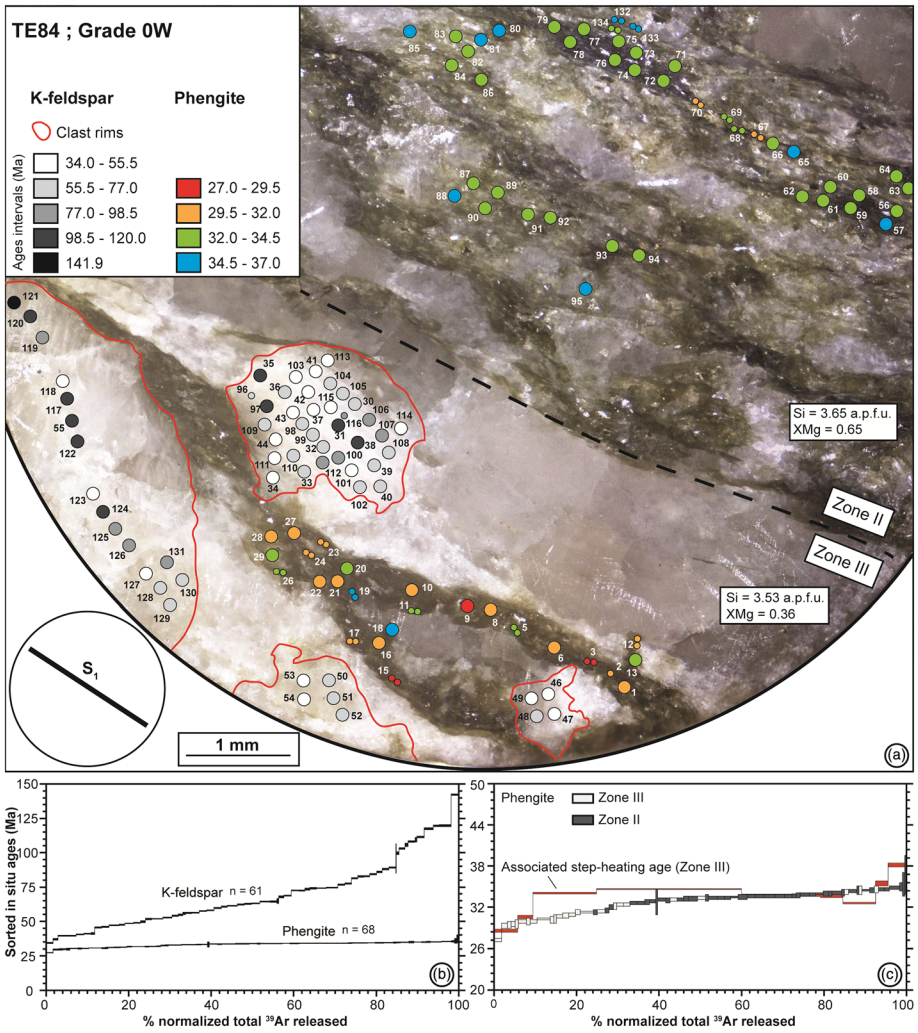

Figure 12. In situ $^{40}Ar/^{39}Ar$ dating of phengite and K-feldspar on section TE84, Grade 0W. (a) Distribution of in situ ages, color scaled for phengite and gray scaled for K-feldspar (grains are contoured in red). In situ ages in phengite are older (~32–37 Ma) in zone II, characterized by the highest mean X_{Mg} than in zone III (~27–32 Ma), characterized by the lowest mean X_{Mg}. Besides, they are randomly distributed in each zone. In situ ages in K-feldspar are randomly distributed but older (~35–150 Ma) than ages in phengite. (b) Spectra of sorted in situ ages for K-feldspar and phengite. (c) Close-up of the phengite spectrum. In red, the step-heating spectrum of TE84Y (zone III) for comparison.

7.2.2. Grade 1 (Meta-Granite TE62)

Section TE62 (Figure 13) exposes S_1 formed by alternating phengite and quartz-feldspar layers, crenulated between S_2 cleavage oriented at 80° clockwise from the horizontal of the picture (Figure 13a). S_2 is thicker (20–50 μm) in the bottom left corner of the analyzed zone and displays recrystallized phengites (see BSE image, Figure 13b) enriched in Al compared to S_1-phengite (see Al composition map in Figure 13c); 100 analyses were acquired on phengite, 50 along S_1 and 50 along S_2. In situ ages range from 33.4 ± 1.0 to 42.6 ± 0.5 Ma (Figure 13a). A slight correlation can be observed between age and microstructures with the oldest ages (40.5–43.0 Ma) spatially associated with S_2-type phengite and the youngest ages (33.0–35.5 Ma) to S_1-dominated microlithons. Intermediate ages follow this trend; 70% of the data fall between 38.0 and 40.5 Ma and are related to S_2 structures. Younger intermediate ages (35.5–38.0 Ma) are evenly distributed among S_1 and S_2. The spectrum of sorted ages is discordant and can be divided in two parts (Figure 13d). The first one increases regularly from ~35.5 to 38.5 Ma between 1% and 82% of cumulative increase. The spectrum then increases nonlinearly from ~38.5 to 43 Ma between 82% and 100% of cumulative increase. Past 80%, the spectrum is mostly dominated by S_2-tied phengite ages.

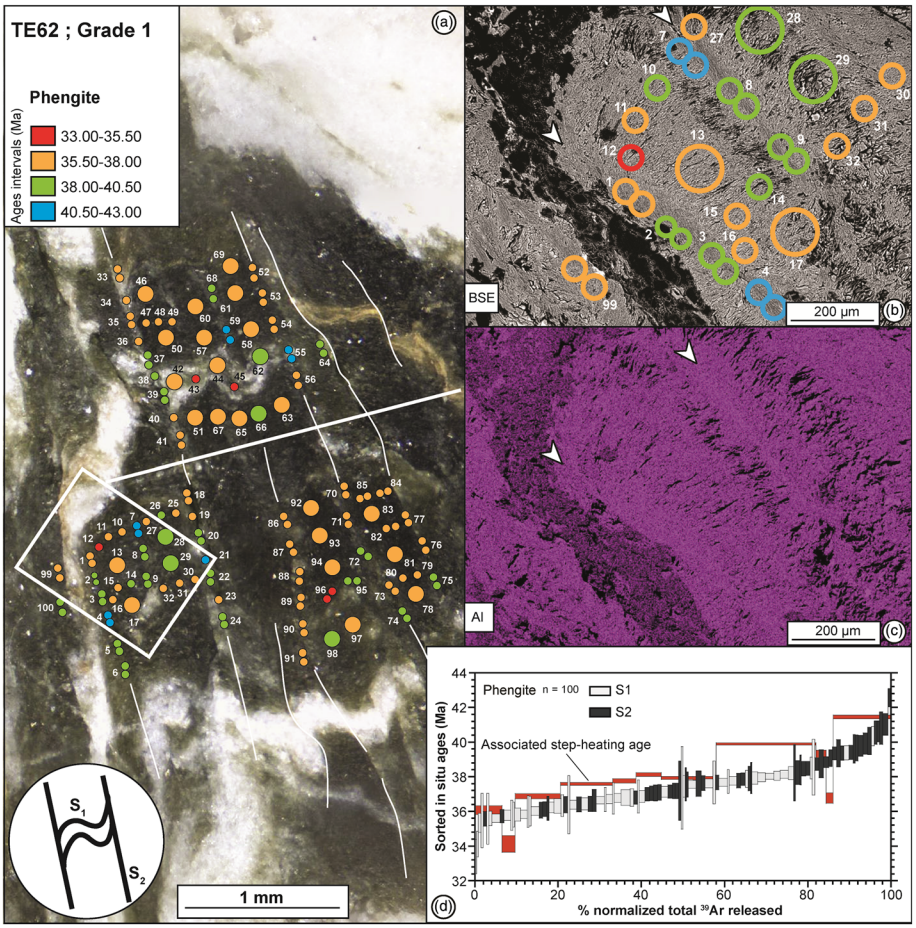

Figure 13. In situ $^{40}Ar/^{39}Ar$ dating of phengite on section TE62, Grade 1. (a) Distribution of in situ ages shows statistically older ages (~38–43 Ma) in S_2 than in S_1 (~33–38 Ma), particularly in the framed bottom left zone (b), the two structures being characterized by slightly different chemical composition exemplified by Al (c), more concentrated in S_2. (d) Spectrum of sorted in situ ages. In red, the step-heating spectrum of TE62B for comparison.

7.2.3. Grade 4 (Meta-Granite TE77)

Section TE77 (Figure 14) is made of finely alternating phengite and quartz-feldspar layers that experienced significant simple shear. Two orientations can be observed, with the dominant S_2 fabric defining the compositional layering and C_2 shear bands developed at an angle of 20° (Figure 14a). Crystals are almost completely transposed in those structures but some of them appear oblique (see BSE image in Figures 14b and 14d). These have a similar chemical composition to layer-parallel phengite grains (see Al composition map in Figure 14c); 74 analyses were acquired on phengite, 23 in layer-parallel crystals carried by S_2, 46 in C_2-parallel crystals, and five in oblique crystals. Ages span from 23.7 ± 1.6 to 33.6 ± 0.5 Ma with no apparent correlation with microstructures (i.e., S_2 versus C_2). Note however that ages in oblique crystals belong to the oldest interval (30.5–34.0 Ma; Figure 14e). Spectrum of sorted ages increases regularly from ~27 Ma to 31.5 Ma between 2% and 90% of cumulative increase (Figure 14e). Beyond, the apparent ages rise more sharply to ~34 Ma.

8. Discussion

8.1. Potential Ar Reservoirs

Before establishing the relationships between deformation, texture, and $^{40}Ar/^{39}Ar$ ages, the coexistence of possibly different Ar reservoirs must be addressed, especially in the case of the step-heating data from the phengite aggregates. While the principal Ar reservoir is obviously phengite, other components may also contribute to the degassing, including in particular the K-feldspars represented by large igneous porphyroclasts (Figure 12) and fine (<50 µm) microcline rims around porphyroclasts of metamorphic albite in Grade 0W

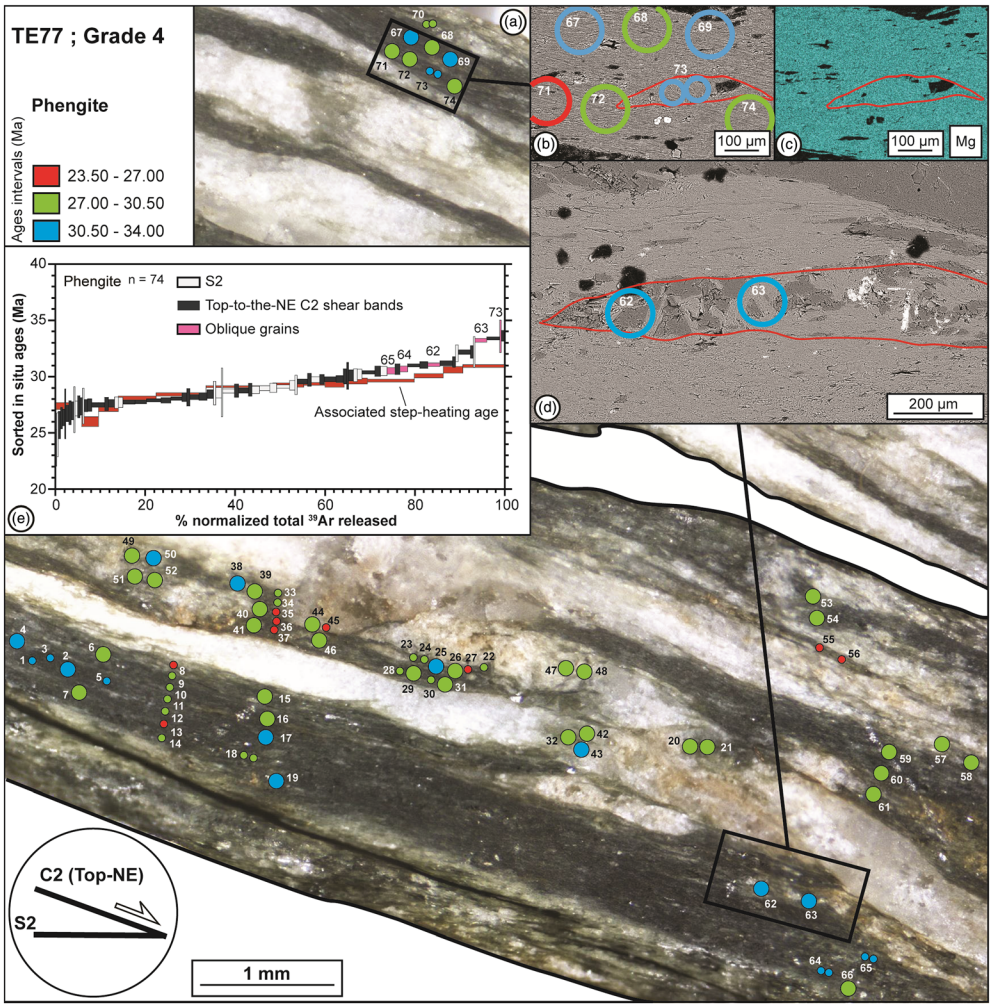

Figure 14. In situ $^{40}Ar/^{39}Ar$ dating of phengite on section TE77, Grade 4. (a) Distribution of in situ ages that are globally randomly distributed in transposed grains in either S_2 or C_2 shear bands (~25–35 Ma). Oblique grains in un-transposed zone surrounded in red (b, d) are however associated with the oldest ages (~30–35 Ma) without significant variation in chemical composition (c). (e) Spectrum of sorted in situ ages. In red, the step-heating spectrum of TE77C for comparison.

samples (see Maggi et al., 2014). The incorporation of igneous K-feldspar in phengite aggregates used for step-heating can be excluded due to its large size. Likewise, the presence of metamorphic microcline appears unlikely because of its scarcity (in any case, its contribution should be very minor considering the volume of the analyzed aggregates). This is even more so in the case of the higher strain grades, where the igneous K-feldspar is totally consumed and metamorphic microcline occurs as localized traces. Other potential contaminants are Cl- or Ca-rich minerals including chlorite or epidote (or fluids trapped as inclusions) as found in some samples. These occur mostly as very small, rare, and localized grains rather than disseminated crystal spatially associated with mica. Experimental $^{38}Ar/^{39}Ar$ (Cl/K) and $^{37}Ar/^{39}Ar$ (Ca/K) ratios are close or within error of zero however, ruling out significant contribution from such phases (see the supporting information). We infer that the age spectra are largely dominated by the degassing from phengite and that the contribution from subsidiary reservoirs such as K-feldspar or impurities is negligible.

8.2. Bracketing Constraints on Age-Deformation Relationships

In the light of potential contamination with excess Ar and/or inheritance, establishing whether the observed ages variations are directly interpretable in terms of age-deformation relationships first requires to bracket the temporal range allowed by independent dating constraints in the Tenda massif (see Figure 3).

A maximum age for alpine metamorphism can be estimated near the end of the Paleocene (~53 Ma), as Eocene sedimentary rocks (dated by correlation with similar facies in Alpine Corsica) are metamorphosed (Rossi et al., 2001). This is consistent with the oldest radiometric ages obtained in the Tenda massif such as the U/Pb-rutile age at 48 ± 18 Ma, together with the aegyrine-phengite U/Pb systematics at 53.7 ± 7.7 Ma of Maggi et al. (2012). Besides, Rb-Sr ages on phengites from top-to-the-SW shear zones constrain the end of D_1 at 30.8 ± 4.2, 31.8 ± 1.7, and 31.5 ± 2.5 Ma (see Figure 1; Rossetti et al., 2015). All these data bracket the permissible age span for D_1 between 50 and 27 Ma. Concerning D_2, Rossetti et al. (2015) have provided a 20.2 ± 2.2 Ma age from a greenschist-facies, highly sheared top-to-the-NE shear zone, constraining the end of the top-to-the-NE deformation stage (see Figure 1). This is consistent with the cooling tempo provided by low-temperature thermochronology. ZFT and AFT yielded scattered ages between 25 and 20 Ma and between 23 and 14 Ma, respectively (Cavazza et al., 2001; Danisik et al., 2007; Fellin et al., 2006; Zarki-Jakni et al., 2004), indicating a fast cooling event during final exhumation through the closure-*T* for the two systems (310°C and 110°C, respectively; Stockli, 2005). Considering the paucity of brittle structures and the lack of brittle increment of deformation over the main shear zones (Beaudoin et al., 2017), these data bracket the end of D_2-deformation in the ETSZ between 25 and 20 Ma at the upper limit of the viscous-brittle transition near 300°C.

Altogether, these bracketing constraints (50–20 Ma) indicate that the ~20 Myr age range spanned by our $^{40}Ar/^{39}Ar$ data (45–22 Ma) and previous $^{40}Ar/^{39}Ar$ data (37–34 Ma, Mailhé, 1982; 35–31 Ma, Jourdan, 1988; 47–25 Ma, Brunet et al., 2000) potentially represents genuine alpine ages unscathed from excess or inherited ^{40}Ar. Brunet et al. (2000) discussed the possible occurrence of excess argon due to local (in situ) ^{40}Ar inheritance commonly affecting H*P*-L*T* reworked pre-Alpine intrusives (e.g., Arnaud & Kelley, 1995; Monié, 1990; Scaillet, 1998). However, this does not seem to apply to our data as shown by the stark age contrast between the matrix phengites and the relic K-feldspars in meta-granite TE84 (Figure 12). These do not overlap at all, with a neatly defined knickpoint at ~35 Ma separating the two in the spectrum of sorted ages (Figure 12). This strongly suggests that the Variscan $^{40}Ar^*$ component released from magmatic K-bearing minerals was efficiently driven off during partial recrystallization at H*P*-L*T* conditions.

Based on these premises, we discuss in the two next sub-sections the mechanisms of mica deformation and their possible interactions on the phengite $^{40}Ar/^{39}Ar$ record.

8.3. Mechanisms of Mica Deformation

Despite the intense deformation recorded by the Tenda massif, phengite crystals appear poorly internally deformed (Figure 5). They dominantly reflect syn-tectonic growth producing newly formed aggregates with a crystallographic preferred orientation (Etheridge et al., 1974; Vernon, 1977), in keeping with studies showing that fabric-forming micas in mylonites are generally strain free (Behrmann, 1984; Etheridge et al., 1974; Wilson & Bell, 1979). Indeed, in this configuration, (001) is sub-perpendicular to the maximum stress axis promoting internal deformation by dislocation glide on (001) associated with gently bended/folded (001), kink boundaries between misoriented (001) domains (Figure 5b) or fracturing, rather than by kink band development or high amplitude folding (Behrmann, 1984; Bell et al., 1986; Bell & Wilson, 1981; Mares & Kronenberg, 1993; Wilson & Bell, 1979). The lattice preferred orientation is stronger in more deformed sample (compare Figure 5g/5h with Figure 5a). This cannot be achieved by dislocation creep because dislocation climb is limited in mica due to the limited number of slip systems. Moreover, slight bending or kinking as observed in Grade 0W is no longer observed in stronger strain grades, indicating that dislocation glide is not an important mechanism. As an example, the folded S_1 in Grade 1 is not represented by folded/kinked grains but by a sequence of strain-free grains that are progressively misoriented from each other toward S_2 (Figure 5f). This observation is reported by Bell and Wilson (1981) in biotite where fracturing along and across (001) is responsible for grain segmentation without dislocations rearrangement, achieving the same result as recovery (i.e., segmentation of several grains misoriented from each other). The fact that grain thickness (but not grain size, as measured along (001)) is reduced implies a strong component of segmentation along (001). In parallel, aggregates record crystallization of new grains and overgrowth, as shown by grains oriented along S_2 (Figure 5f) or thin but large grains (up to 400 μm) aligned along shear bands (Figure 5i). This calls for an important participation of dissolution/precipitation processes. These are evidenced by serrated boundaries and the nucleation/growth of mica in boundaries and triple junction of

albite and quartz (Figures 5h, 5j, 5l, and 7a), attesting to solute transfer by advective transport of components for mica nucleation. Consequently, in Grades 1 to 4, competing grain size growth and reduction mechanisms led to a continuous alignment of (001) along structures (i.e., folded S_1, S_2, and C_2) but without significant reduction in overall grain size distribution (Table 1).

Tracking sequential changes in the fabric development through the deformation sequence (and grades) is rendered difficult due to the isochemical behavior of white mica across during deformation and the lack of other diagnostic phases to delineate discrete changes through the *P-T-strain* history. The different phengite generations appear compositionally similar with inter-sample variations chemically buffered by the bulk-rock composition rather than by temporal *P-T-strain* changes (the more ferromagnesian the protolith, the more ferromagnesian the phengite; see Figure 6). The lack of extra ferromagnesian phase for cation exchange in an overall mineralogically stable assemblage partly explains such a bulk-compositional effect (Table 1). However, mass-balance calculations indicate pervasive fluid-rock exchange in the study area (Maggi et al., 2014), the phengite composition primarily reflecting the mineralogical transformations attending D_1 under the (local) control of protolith variations, *P-T* conditions, and external fluid availability. These data indicate that the bulk mineralogy, the phengite composition, and the phengite amount were acquired early during D_1 after the total consumption of magmatic ferromagnesian minerals. Once consumed, the lack of such reactants precluded further mineralogical exchange, explaining why samples deformed during D_2 dominantly consist of aggregates of pre-existing D_1 grains. Relic core compositions in core-rim zonations (Figure 7; Table 1) may be linked to early local equilibrium reflecting early (pre- to syn-D_1) mineral transformations. These microtextures are clear, homogeneous, and concentric in D_1 samples (Figures 7d–7f), indicating that early crystal growth is the main fabric-forming process of mica aggregates at this stage. Conversely, chemical zonation appears patchy, heterogeneous (asymmetric and discontinuous) in D_2 samples (Figure 7j) and is interpreted as truncated relic of early (syn-D_1) growth zonation. Accordingly, we infer that recrystallization processes during D_2 deformation occurred without major within-grain chemical equilibration but rather via dissolution-precipitation assisted by some grain-boundary fluid. Accordingly, nucleation of new grains does not necessitate a change in chemical composition as a driving force (Behrmann, 1984).

Summarizing, textural relationships across the deformation sequence indicate that after a first phase of crystal growth and coarsening during D_1, phengite aggregates recorded continuous deformation until almost complete transposition of former fabrics during D_2 without significant crystal-scale re-equilibration, nor bulk grain size reduction past Grade 0W. How these mineral deformation and recombination processes interacted with the $^{40}Ar/^{39}Ar$ isotopic record is addressed in the next sub-section.

8.4. Mechanisms of ^{40}Ar Isotopic Record During Progressive Deformation

Four main mechanisms can be responsible for the age younging with deformation, as evidenced by our data: (1) Ar transfer via fast-pathway pipe diffusion or cross-lattice defects activated at lower temperature than volume diffusion (e.g., Cosca et al., 2011; Hames et al., 2008; Kramar et al., 2001, 2003; Lee, 1995; Lo et al., 2000). (2) Dynamic sub-grain size refinement reducing the effective diffusion length scale and closure-*T* (e.g., Cosca et al., 2011; Dunlap & Kronenberg, 2001; Goodwin & Renne, 1991; Mulch et al., 2002). (3) Partial to full recrystallization inducing variable resetting and mixing with incompletely reset precursory grains (e.g., Augier et al., 2005; Dunlap, 1997; Dunlap & Kronenberg, 2001; Kirschner et al., 1996; Scaillet et al., 1990; West & Lux, 1993). (4) Crystal-scale dissolution/precipitation replacive changes assisted by an intergranular free fluid phase (fluid-assisted diffusional creep; see Scaillet, 1996, 1998).

As discussed in section 8.3, there is no evidence for higher density of defects at increasingly higher strain grade. Basal parting along (001) dominates over grain segmentation across (001) and cannot bring about a reduction of effective diffusion length (and closure-*T*) if volume diffusion occurs primarily along the mica interlayer. Thus, deformation-enhanced Ar loss by mechanisms (1) and (2) cannot explain alone the age variations between the different strain grades, calling for mechanisms (3) and (4) as the dominant processes to explain the patchy and irregular age distribution and trends observed at all scales. This is consistent with an important participation of dissolution-precipitation in deformation of mica aggregates, as already evidenced in section 8.3 and discussed in recent studies (Airaghi et al., 2017; Berger et al., 2017). This may allow compositional re-equilibration at temperatures below which static (solid-state) diffusion of major elements becomes ineffective (e.g., Dempster, 1992). A related form of fluid-phase diffusional creep (or fluid-

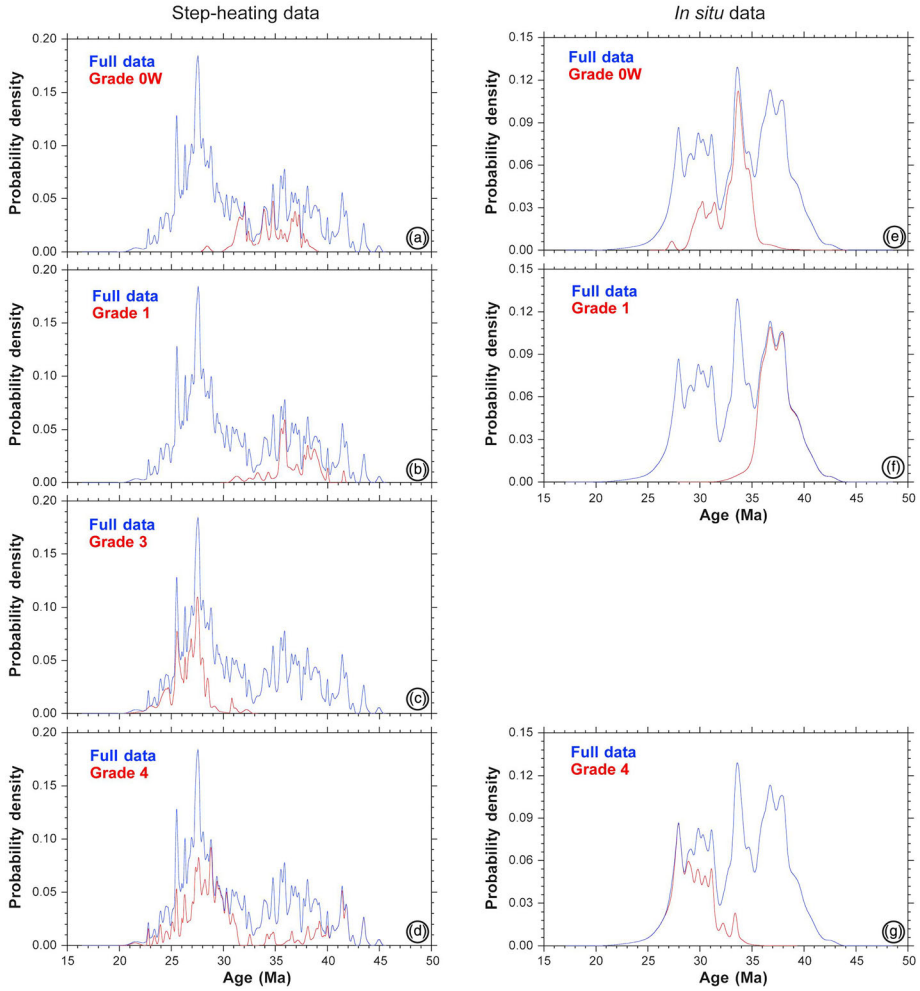

Figure 15. Results of the PDD analysis per strain grade for step-heating (left column) and in situ (right column) dating. See text for further explanations.

assisted dissolution-precipitation creep) operating in the ductile regime has already been argued as a major driver for Ar re-mobilization with partial or total resetting of $^{40}Ar/^{39}Ar$ ages below the nominal closure-*T* for Ar loss by diffusion in micas (Scaillet, 1996, 1998).

8.5. Multi-Factorial Analysis of Age Versus Deformation Relationships

In order identify possible cause-and-effect relationships between field observations, finite-strain fabrics, and apparent ages, we devise below a multi-parametric analysis relating all observables with the mapped age trends and local-scale $^{40}Ar/^{39}Ar$ systematics.

8.5.1. PDD Analysis

Data were plotted as a probability density distribution (PDD) summing the individual Gaussian density of every datum (Figure 15), providing a continuous kernel density spectrum from which characteristic peaks, or frequency groups, can be tentatively assigned to one (or more) strain grade(s). Because the system studied is temporally dynamic and spatially heterogeneous, we devise below a global trend analysis based on such empirical PDD patterns to correlate the age variations with the observables (structural position, strain grade, grain size, and geochemistry) collected via our multi-scale, multi-parametric approach.

In attempting to integrate the observations into a coherent model of age versus deformation relationships, we must account for the following features.

1. The majority of the age spectra is variably and erratically discordant with no coherent trend or systematic increase during degassing (Figures 8–11). The lack of systematic correlation between internal discordance and $^{40}Ar/^{39}Ar$ spectrum shape prohibits assigning a single mechanism, like partial loss/resetting by diffusion, to the trends. We interpret such spectra as mixed-reservoirs patterns reflecting the differential degassing of structurally thermally distinct domains rather than diffusion-driven experimental kinetics.
2. There is an overall agreement in terms of internal discordance between the in situ data and step-heating systematics (compare them in Figures 12–14), indicating that the latter do preserve a faithful record of internal $^{40}Ar/^{39}Ar$ gradients.
3. As noted before, thermal-diffusional effects during the H*P*-L*T* cycle were unable to completely erase the pre-Alpine signature of magmatic K-feldspar while the phengite ages are distinctly Alpine in origin in the same lithology; the stark age contrast between these two phases directly matches the overprinting textural relationships, indicating that $^{40}Ar/^{39}Ar$ systematics in the phengites are kinetically controlled by recrystallization in the matrix phase rather than by diffusion alone.

Motivated by observation (2), we assume in what follows that any mixing effect of within-grain components (reservoirs) degassed during step-heating is subordinate and that the internal age gradients are preserved such that each individual step-age indirectly relates to a true discrete event (e.g., closure/crystallization or resetting age). Minimal experimental mixing (i.e., averaging) is also suggested by the mutually discordant replicates from the same samples (e.g., TE61B in Figure 8) indicating that the step-heating data do retain a representative record of internal $^{40}Ar/^{39}Ar$ discordance. Accordingly, the $^{40}Ar^*$ gradients manifested by the discordant age spectra are approximated to reflect distinct (discrete) phengite generations or subdomains with a characteristic closure or (re)crystallization age. Specifically, we evaluate a model whereby the experimental $^{40}Ar/^{39}Ar$ spectra reflect the time-integrated, incremental growth/recystallization stages experienced by the samples and that the pooled analysis of the individual age distributions across the sample suite provides a way to extract regionally meaningful trends beyond sample-specific or local effects. The relevance and implications of such assumptions are discussed later.

The full PDD spectrum relative to step-heating ages (Figure 15, left column) pooling all strain grades displays two peaks culminating near 36 Ma (Mode I) and 27 Ma (Mode II), with second-order satellite peaks erratically distributed throughout. Grade 0W is clustered in the mid of the range (30–40 Ma), with a multi-modal pattern showing no dominant component (Figure 15a). Grade 1 displays a spectrum coinciding with mode I of the pooled spectrum (Figure 15b). Grade 3 is concentrated at the younger end of the record with a dominantly unimodal and symmetric peak contributing exclusively to Mode II (Figure 15c). In contrast, Grade 4 is dominantly bimodal and skew-asymmetric with a tail of apparent ages fading away from both modes toward younger ages (Figure 15d). While the younger maximum coincides and contributes significantly to the pooled Mode II, the second peak at ~41 Ma is distinctly older than Mode I and is unique to this category. This older component is carried by one single sample, TE41, displaying the oldest ages of the suite (Figure 9).

Applied to the in situ data, the spectral PDD analysis reveals a less noisy pattern over a duration spanning the same length (20–44 Ma, Figure 15, right column). Grade 0W shows a dominant mode peaking at ~33–34 Ma centrally located relative to the full distribution, with a second order peak near 29–32 Ma (Figure 15e). Grade 1 plots at the older end with a dominantly unimodal peak at 37–38 Ma with a neutral polarity trend (Figure 15f). Grade 4 defines the youngest component of the full record sharply peaking at ~28 Ma (Figure 15g) with a second order peak near 32–34 Ma.

8.5.2. MCP Analysis

To inquire further into possible age versus deformation relationships, the PDD analysis can be coupled with mixed-coefficient parameter spectra to illustrate how much a given sample characteristic or category (strain grade, geochemistry, sample location, and grain size) is associated to a given pooled age—or temporal bandwidth—across the PDD. Mixed-Coefficient Parameter (MCP) spectra (Figure 16) are computed by weighing pointwise a parameter or category attached to each individual age by the corresponding age-density kernel across the PDD, then by summing over the full age distribution and normalizing by the local PDD. As such, they provide a density-weighted estimate of a given parameter contribution across the PDD spectra using a continuous ordinal scale. While intermediate values across this scale do not strictly represent true (continuous) transitional variations between potentially discrete or categorical values (e.g., like the ordinal strain

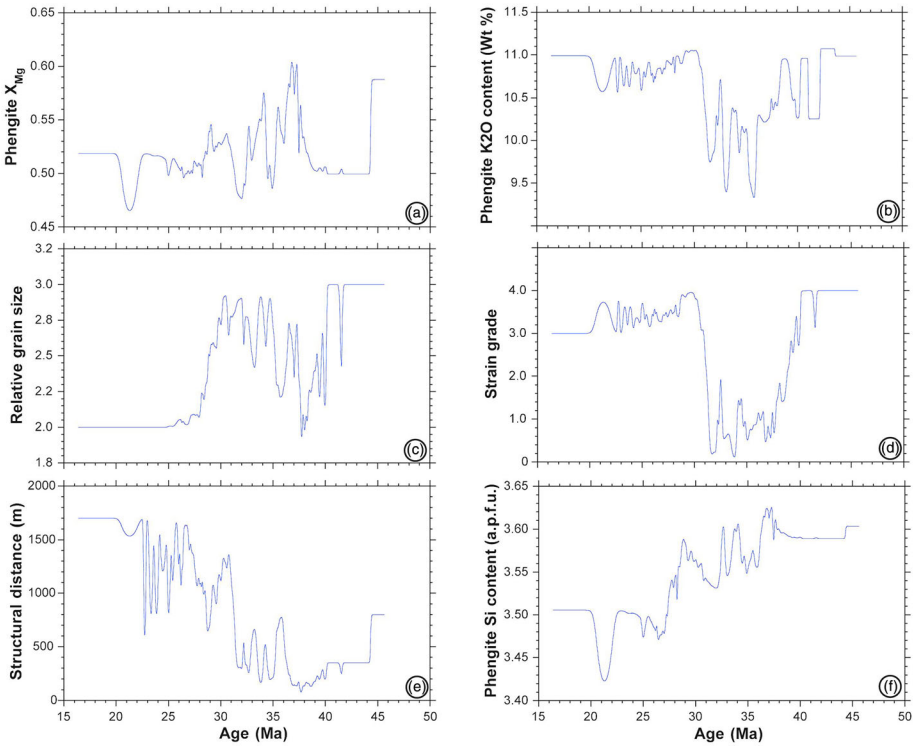

Figure 16. Results of the MCP analysis. See text for further explanations.

grade), such a construct potentially provides a semi-quantitative estimate of the mixed-magnitude contribution of a given parameter provided the age depends continuously on that parameter. For instance, strain grades are defined by discrete, ordered, values (categories). Implicit in the transition from Grade 0W through Grade 4 is the concept of cumulative finite strain due to the incremental (continuous) development of the shear fabric. Grades are ordered through a relative scale scoring the magnitude of the associated deformation through such a continuum and the continuous MCP plot smoothes out the transition between these categories according to the age probability attached to a given grade. For this as for any physically continuous parameter, this display affords a practical way to reveal coupled age-parameter variations (or lack thereof) that would be difficult to correlate across the temporal series otherwise.

Overall, the MCP compositional plots for X_{Mg} (Figure 16a) and K_20 (Figure 16b) indicate no correlation with age variation. One local exception is suggested by the in situ ages in section TE84 displaying older high-X_{Mg} (0.65 ± 0.06, ~34 Ma) phengites in zone II and younger low X_{Mg} (0.36 ± 0.04, 29–34 Ma) phengites in zone III (Figure 12). Mg-rich micas are empirically considered more retentive than Fe-rich endmembers (Dahl, 1996; Harrison et al., 1985; Scaillet et al., 1992) and the older ages at ~34 Ma of the Mg-rich specimens of zone II could potentially point to lower-retention closure ages. However, this effect has been noted for this sample only and cannot explain the regional trends. Such a lack of control by X_{Mg}, along with the lack of correlation between grain size and ages (Figure 16c), strengthen our assumption that Ar lattice (volume) diffusion did not dominate the phengite $^{40}Ar/^{39}Ar$ record, as stated earlier (sections 8.4 and 8.5.1). Likewise, a K-loss (pyrophyllite) effect on $^{40}Ar/^{39}Ar$ ages could be suggested by sample TE62 (Figure 13) which displays syn-S_2, pyrophyllite-rich, phengites (see depletion in K, Figure 7g) older than earlier syn-S_1 phengites. Such reverse discordance could be attributed to recoil loss of ^{39}Ar from the K-poor pyrophyllite intermixed within phengite. In the same way as for chloritized biotite, this could bias the apparent age via a combination of ^{39}Ar recoil into K-poor domains (Di Vincenzo et al., 2003; Lo & Onstott, 1989) with ^{39}Ar loss from the low-retentive low-K domains during irradiation (e.g., Hess & Lippolt, 1986). We note however that such a correlation is not systematic. For instance, while phengites TE41 and TE52 are characterized by a high pyrophyllite

component (Figure 6b), only the first is associated with apparently older ages relative to the rest of the data set (see section 8.5.1 and Figures 9 and 11). Thus, a systematic and direct correlation between K content and age can also be dismissed.

In contrast, a control of deformation is clearly highlighted by the temporal strain distribution revealed by the MCP analysis. High strain grades (Grades 3 and 4) and low strain grades (Grades 0W and 1) rocks, respectively localized toward the (northeast) upper parts and the (southwest) lower parts of the ETSZ, are respectively associated with the youngest (<30 Ma) and oldest (>30 Ma) ages (Figures 8–11). This is clearly expressed by the MCP spectrum of strain grades (Figure 16d) with the first half (youngest ages) dominated by oscillations between Grades 3 and 4, the second one (oldest ages) dominated by Grades 0W and 1. The MCP plot of the structurally projected distance (Figure 16e) of each sample onto a virtual cross-sectional plane oriented SW-NE (with an origin arbitrarily set to the deepest sample) reveals a clear polarity trend with an oscillatory younging toward the northeast. While the present-day relative position in the structural stack may be locally offset by late faults or may not be representative of a purely cylindrical deformation field, such a pattern is strongly suggestive of the progressive localization of deformation in that direction through the 40–20 Ma timespan. Interestingly, a bulk antipathetic trend is manifested by the Si-phengite MCP plot showing an oscillatory-like decrease in Si-content in this age range (Figure 16f), consistent with progressively shallower lithostatic pressures in the corresponding time interval, although the Si-content may be partly buffered by the host rock composition.

8.6. Regional Implications

The PDD analysis indicates a deformation continuum between 40 and 20 Ma with two major episodes culminating near ~35–36 Ma (Mode I) and ~27–28 Ma (Mode II) and secondary events scattered throughout (Figure 15). Compositional and grain size effects, as well as structural inheritance from earlier pre-Alpine (magmatic) fabric, appear quite marginal in controlling the bulk phengite age distribution. The latter appears dominated by the spatio-temporal development of the deformation sequence recorded across the whole Tenda unit. Mode I and Mode II are respectively represented by Grades 0W–1 and Grades 3–4. These are respectively characterized by S_1/L_1/top-to-the-SW (and minor S_2) and S_2/L_2/top-to-the-NE structures. These relationships bear on the attribution of D_1 and D_2 structures respectively to burial and exhumation, and the timing of their transition. Mode I and Mode II are separated by a probability deep at 33–34 Ma in the full PDD spectra (Figure 15). Noteworthy, part of the internal Schistes Lustrés nappe was in the burial stage close to the peak-pressure at this stage (Martin et al., 2011; Vitale Brovarone & Herwartz, 2013). This was the case of the Tenda massif as well assuming that top-to-the-SW shearing in the ETSZ accommodated burial (rather than exhumation and cooling) contemporaneously in the crustal wedge. That this date is possibly very close to the age of maximum burial is suggested by the minimum $^{40}Ar/^{39}Ar$ ages near 34–35 Ma in K-feldspar of sample TE84 (Figure 12). These are equal to the maximum age of crystallization of the coexisting Alpine phengite and thus correspond to the most severely (if not totally) reset K-feldspar ages during peak-T metamorphic conditions prior to subsequent closure and accumulation of ^{40}Ar due to the combined effects of temperature decrease during incipient exhumation and cessation of local deformation. On the other hand, the start of exhumation in the most external alpine deformation zones (i.e., Variscan basement of central Corsica) is constrained at ~33 Ma, marking the beginning of exhumation of the whole nappe stack, including the Tenda massif (Di Vincenzo et al., 2016). Following the interpretation of Beaudoin et al. (2017) and in light of these new data, D_1 structures (S_1/L_1/top-to-the-SW) and D_2 structures (S_2/L_2/top-to-the-NE) can be respectively attributed to burial and exhumation culminating at ~35–36 Ma (Mode I) and ~27–28 Ma (Mode II), with a switch at ~34 Ma. This is consistent within error bars with the top-to-the-SW/top-to-the-NE switch independently constrained by Rb-Sr ages (Rossetti et al., 2015). This tectonic inversion/reactivation occurred when Corsica passed from an east-dipping Alpine subduction geometry to a back-arc domain setting with the development of the west-dipping Apennine subduction system near 35–30 Ma (Malusà et al., 2015; Molli & Malavieille, 2011). The coincidence between the D_1/D_2 switch and the low probability of the full PDD spectrum at 33–34 Ma (Figure 15) strongly suggests a low amount of strain and recrystallization at this time consistent with more distributed deformation during the tectonic switch (Beaudoin et al., 2017; Molli et al., 2006). The preservation of such an age sequence also suggests minimal mixing of the different age components during incremental $^{40}Ar/^{39}Ar$ degassing, as previously argued.

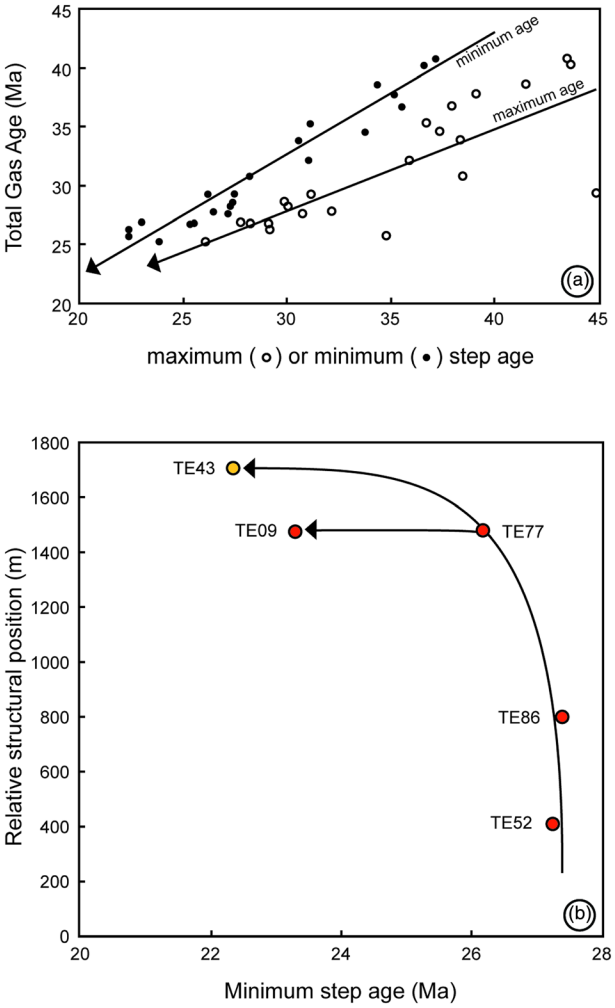

Figure 17. Global age trends. (a) Maximum/minimum recorded age versus total gas age. (b) Minimum recorded ages versus structural position. Note that for minimum ages, the first step is not considered.

While age mixing is believed to be very limited, we recognize that it can affect to a variable extent the data, primarily in the form of grain-scale disequilibrium brought about by incomplete recrystallization in the absence of efficient thermal drive for Ar diffusion and resetting. The crux observations in this connection are twofold. (1) There is no correlation between extent of deformation (grade) and internal $^{40}Ar/^{39}Ar$ scatter. (2) The latter is preserved both as aggregate-scale $^{40}Ar/^{39}Ar$ gradients related to aggregate-scale textures (see the relative old oblique S_1 crystals in TE77 in Figure 14) and as grain-scale $^{40}Ar/^{39}Ar$ gradients unrelated to grain-scale textures due to dissolution-precipitation replacive changes. Accordingly, we interpret the progressively reduced maximum and minimum ages with decreasing total-gas age (Figure 17a) as the effect of a juvenile fabric being progressively formed with a decreasing contribution from early-formed micas. Considering that $^{40}Ar/^{39}Ar$ systematics in the phengites (1) are kinetically dominated by recrystallization (rather than by diffusion) in the matrix phase and (2) that they reflect mixing of distinct phengite generations, the youngest steps give a maximum age for the end of deformation in a given sample while the oldest ones gives a minimum age for the start of deformation (e.g., Beltrando et al., 2009; Wijbrans & McDougall, 1986).

Accordingly, the ages of the youngest steps recorded herein at ~22 Ma indicate the maximum age for the end of deformation in the ETSZ, which again is slightly older (but still consistent within error bars), with the Rb-Sr ages and interpretation of Rossetti et al. (2015). Considering (1) that such a young age is consistent with low-temperature thermochronologic data between 300°C and 100°C and (2) the paucity of brittle structures, these data indicate that the deformation in the ETSZ ended in the uppermost parts of the viscous/brittle transition. Taken together, the D_1/D_2 switch at ~34 Ma and the end of D_2 at ~22 Ma return a ~12 Myr timelife for the ETSZ as a top-to-the-NE extensional shear zone. This is a minimal duration for regional strain localization. This timelife falls in the range of reasonably known durations of shear zone activity constraints (e.g., Beaudoin et al., 2015; Brichau et al., 2006; Charles et al., 2013; Duchêne et al., 2006; Schärer et al., 1994; Schneider et al., 2013; Turrillot et al., 2011). In keeping with previous models (Beaudoin et al., 2017; Daniel et al., 1996; Gueydan et al., 2003; Jolivet et al., 1990, 1991; see section 2.2), this duration, together with the D_2 structures pervading the ETSZ (Figure 2; Beaudoin et al., 2017), denotes this structure as a major top-to-the-NE post-orogenic extensional shear zone rather than as a local short-lived reactivation.

In terms of strain localization, the spatial distribution of the youngest steps of Grade 3–4 samples (Figure 17b) suggests that the latest strain increments during D_2 migrated progressively toward the northeast upper levels. This regional trend follows the large scale strain gradient (Beaudoin et al., 2017) but does not reproduce it exactly. This is attested by Grade-3 (but not Grade-4) samples populating the youngest peak in the full PDD spectrum (compare Figures 15c and 15d). This is also true at the sample scale. For example, resetting down to 22–24 Ma in sample TE43 is not restricted to the more deformed zones but also occurs in early low-strained crenulated zones (Figure 10). Thus, it is worth to note that without age constraints, the use of regional strain gradients as a proxy for strain localization in time may be valid at large scale, but it may be locally invalid within individual shear zones.

Besides the regional strain localization in space and time highlighted by combining structural analysis and $^{40}Ar/^{39}Ar$ systematics, the data also indicate that strain localization follows local effects controlled notably by the type of protolith. This is exemplified by the younger ages in meta-aplite TE09 compared to the nearby meta-granite TE77 (Figure 17b). Thus, $^{40}Ar/^{39}Ar$ dating appears strongly useful to explore strain localization patterns in shear zones characterized by a heterogeneous nature of protolith, as it is difficult in such context to recognize strain gradients, and then infer on strain localization in space.

8.7. Dynamic Closure and $^{40}Ar/^{39}Ar$ Dating of Deformation Across the Viscous/Brittle Transition

The analysis above inherently carries with itself the concept of dynamic closure whereby discrete micas generations may locally record the timing of growth/replacement by dissolution-precipitation, resulting in a mozaic of texturally and isotopically complex crystals bearing no systematic apparent relationship to mineral composition, microstructure, or overprinting textures. Particularly relevant here is the observation that the inferred grain or domain-scale age distribution cannot be directly tied to a specific deformation stage or texture recorded at the sample scale via the in situ approach unless the regional record is properly understood. This is because the processes involved (dissolution-precipitation) can take place decoupled from the local solid-state finite strain record, leaving a texture of undeformed (strain-free) sub-grains or crystal domains formed in an otherwise dynamically forming fabric.

The meaning of the age discordance characterizing such systems may be elusive in settings lacking extensive (in situ and regional) $^{40}Ar/^{39}Ar$ sampling coverage as deployed here. In particular: do such $^{40}Ar/^{39}Ar$ systematics represent a continuum of deformation or a blurred record of discrete events overlapping in time that are successively overprinted to leave just a vestige of mixed ages? The answer probably lies somewhere in between. The fact that the most deformed samples here are not completely homogenized clearly argues in favor of such $^{40}Ar/^{39}Ar$ systematics mostly reflecting intermediate ages of mixed origin. The question thus refers to how well one can relate ages with texture/structure. Our data amply demonstrate that such connection is blurred beyond what standard optical, SEM, and UV-laser probe techniques may presently resolve. The level of crystal-isotope interactions in such systems is rooted into the mica interlayer seen as the preferential pathway for chemical reactivity. Combined with grain-scale gradients in fluid activity and transient changes in permeability/porosity, this greatly contributes to make such systems particularly challenging to date.

In 300–400°C fluid-present systems deforming near the viscous/brittle transition, the concept of dynamic closure supersedes the classic view that a K-Ar system may be simply defined as closed or open with respect to a static, nominally defined, closure temperature. While necessarily empirical, such a conceptual extension opens useful prospects in terms of $^{40}Ar/^{39}Ar$ dating of deformation by incorporating common phenomena such as the catalytic action of fluids, fluid-mineral equilibria, and fluid-rock-deformation feedback relationships that are impossible to rationalize otherwise. In the Tenda case, our integrated $^{40}Ar/^{39}Ar$ approach appears to uncover an isotopic record of deformation lasting for as long as 20 Myr in the temporal range recorded by white mica. It permits to put important constraints in the temporal range recorded by white mica, most notably on the ~12 Myr timelife inferred for extensional motion along the ETSZ. Younging trends have permitted to capture and explore spatio-temporal variations in strain localization at different scales, that are required in rheological works, considering that deformation mechanisms can be strain and time dependent (Fusseis et al., 2006; Fusseis & Handy, 2008; Marti et al., 2017; Pec et al., 2012). However, as it is difficult at small scale to relate ages retrieved in some (micro)structures with the true age of these (micro)structures, along with the mixed ages that might produce intermediate values with no direct geologic meaning, we keep this exploration qualitative.

9. Conclusion

In the light of our $^{40}Ar/^{39}Ar$ multi-scale analysis of the East Tenda shear zone, the following conclusions can be drawn:

1. Intrinsic parameters involved in Ar diffusion including mica composition and grain size do not control the bulk $^{40}Ar/^{39}Ar$ ages, indicating a minimal participation of diffusion. Along with the lack of inherited Ar and the general agreement of ages with independent age constraints, we uncover a direct link between deformation/recrystallization processes and the $^{40}Ar/^{39}Ar$ record at the regional scale.
2. $^{40}Ar/^{39}Ar$ spectra are interpreted as mixed-reservoir patterns reflecting the differential degassing of structurally thermally distinct domains rather than diffusion-driven experimental kinetics. The agreement of internal discordance between in situ and step-heating ages suggests that the later preserve a faithful record of internal $^{40}Ar/^{39}Ar$ gradients and that individual step ages may be indirectly associated to discrete (re-crystallization) events, strengthening the use of the step-heating technique for tracking the deformation tempo recorded by the mica fabric.

3. The data uncover an isotopic record of deformation lasting for over 20 Myr. Key dates around ~34 and ~22 Ma can be assigned to the end of burial and cessation of deformation during subsequent exhumation, respectively; these allow to infer a ~12 Myr timelife of extensional motion along ETSZ until the Tenda massif reached the uppermost parts of the viscous/brittle transition. Regionally, younging trends reveal spatio-temporal variations in strain distribution with progressive localization toward the upper contact of the unit and smaller-scale localization in weak lithologies, notably meta-aplites. Thus, methodically, $^{40}Ar/^{39}Ar$ dating as deployed here offers interesting perspectives if coupled with rheological purposes.
4. The lack of systematic correlation between (i) ages and microstructures and (ii) ages and strain grades indicates that the deformation mechanisms controlling $^{40}Ar/^{39}Ar$ systematics can be decoupled from local solid-state finite strain record. Along with the effects of mixed ages and partial Ar resetting, this invites utmost caution in relating ages to microstructures and inferring rates of strain localization.

Data Availability Statement

Data sets for this research are available online (https://zenodo.org/record/4014973).

Acknowledgments

Federico Rossetti and two anonymous reviewers are thanked for their constructive comments and suggestions that improved the manuscript. This work has received funding from the European Research Council (ERC) under the Seventh Framework Programme of the European Union (ERC Advanced Grant, grant agreement No. 290864, RHEOLITH) and the Institut Universitaire de France. It is also a contribution of the Labex VOLTAIRE. The $^{40}Ar/^{39}Ar$ facility at ISTO was funded and is supported by the ERC Advanced grant RHEOLITH, the LABEX project VOLTAIRE (ANR-10-LABX-100-01), the Région Centre project ARGON, and the project EQUIPEX PLANEX (ANR-11-EQPX-0036).

References

Airaghi, L., Lanari, P., de Sigoyer, J., & Guillot, S. (2017). Microstructural vs compositional preservation and pseudomorphic replacement of muscovite in deformed metapelites from the Longmen Shan (Sichuan, China). *Lithos*, *282–283*, 262–280. https://doi.org/10.1016/j.lithos.2017.03.013

Arnaud, N. O., & Kelley, S. P. (1995). Evidence for excess argon during high pressure metamorphism in the Dora Maira massif (western Alps, Italy), using an ultra-violet laser ablation microprobe $^{40}Ar/^{39}Ar$ technique. *Contributions to Mineralogy and Petrology*, *121*, 1–11. https://doi.org/10.1007/s004100050086

Augier, R., Agard, P., Monié, P., Jolivet, L., Robin, C., & Booth-Rea, G. (2005). Exhumation, doming and slab retreat in the Betic Cordillera (SE Spain): In situ $^{40}Ar/^{39}Ar$ ages and *P-T-d-t* paths for the Nevado-Filabride complex. *Journal of Metamorphic Geology*, *23*, 357–381. https://doi.org/10.1111/j.1525-1314.2005.00581.x

Beaudoin, A., Augier, R., Jolivet, L., Jourdon, A., Raimbourg, H., Scaillet, S., & Cardello, G. L. (2017). Deformation behavior of continental crust during subduction and exhumation: Strain distribution over the Tenda massif (Alpine Corsica, France). *Tectonophysics*, *705*, 12–32. https://doi.org/10.1016/j.tecto.2017.03.023

Beaudoin, A., Augier, R., Laurent, V., Jolivet, L., Lahfid, A., Bosse, V., et al. (2015). The Ikaria high-temperature metamorphic core complex (Cyclades, Greece): Geometry, kinematics and thermal structure. *Journal of Geodynamics*, *92*, 18–41. https://doi.org/10.1016/j.jog.2015.09.004

Beccaluva, L., Ohnenstetter, D., & Ohnenstetter, M. (1981). K-Ar age determination on some Tethyan ophiolites. *Rendiconti della Societa Italiana di Mineralogia e Petrologia*, *37*, 869–880.

Behrmann, J. H. (1984). A study of white mica microstructure and microchemistry in a low grade mylonite. *Journal of Structural Geology*, *6*(3), 283–292. https://doi.org/10.1016/0191-8141(84)90052-X

Bell, I. A., & Wilson, C. J. L. (1981). Deformation of biotite and muscovite: TEM microstructure and deformation model. In: Lister, G. S., Behr, H.-J, Weber, K., Zwart, H. J. (Eds.), The effect of deformation on rocks. *Tectonophysics*, *78*, 201–228. https://doi.org/10.1016/0040-1951(81)90014-7

Bell, I. A., Wilson, C. J. L., McLaren, A. C., & Etheridge, M. A. (1986). Kinks in mica: Role of dislocations and (001) cleavage. *Tectonophysics*, *127*, 49–65. https://doi.org/10.1016/0040-1951(86)90078-8

Bellanger, M., Augier, R., Bellahsen, N., Jolivet, L., Monié, P., Baudin, T., & Beyssac, O. (2015). Shortening of the European Dauphinois margin (Oisans massif, Western Alps): New insights from RSCM maximum temperature estimates and $^{40}Ar/^{39}Ar$ in situ dating. *Journal of Geodynamics*, *83*, 37–64. https://doi.org/10.1016/j.jog.2014.09.004

Beltrando, M., Lister, G. S., Forster, M., Dunlap, W. J., Fraser, G., & Hermann, J. (2009). Dating microstructures by the $^{40}Ar/^{39}Ar$ step-heating technique: Deformation–pressure–temperature–time history of the Penninic units of the Western Alps. *Lithos*, *113*, 801–819. https://doi.org/10.1016/j.lithos.2009.07.006

Berger, A., Wehrens, P., Lanari, P., Zwingmann, H., & Herwegh, M. (2017). Microstructures, mineral chemistry and geochronology of white micas along a retrograde evolution: An example from the Aar massif (Central Alps, Switzerland). *Tectonophysics*, *721*, 179–195. https://doi.org/10.1016/j.tecto.2017.09.019

Bézert, P., & Caby, R. (1988). Sur l'âge post-bartonien des événements tectono-métamorphiques alpins en bordure orientale de la Corse cristalline (Nord de Corte). *Bulletin de la Societe Geologique de France*, *4*, 965–971.

Bézert, P., & Caby, R. (1989). La déformation progressive de l'Eocène de la région de Corte: nouvelles données pétrostructurales et conséquences pour la tectogenése alpine en Corse. *Comptes Rendus de l'Academie Des Sciences de Paris*, *301*(1), 95–101.

Brichau, S., Ring, U., Ketcham, R. A., Carter, A., Stockli, D., & Brunel, M. (2006). Constraining the long-term evolution of the slip rate for a major extensional fault system in the central Aegean, Greece, using thermochronology. *Earth and Planetary Science Letters*, *241*, 293–306. https://doi.org/10.1016/j.epsl.2005.09.065

Brunet, C., Monié, P., Jolivet, L., & Cadet, J. P. (2000). Migration of compression and extension in the Tyrrhenian Sea, insights from $^{40}Ar/^{39}Ar$ ages on micas along a transect from Corsica to Tuscany. *Tectonophysics*, *321*, 127–155. https://doi.org/10.1016/S0040-1951(00)00067-6

Cardello, G. L., Di Vincenzo, G., Giorgetti, G., Zwingmann, H., & Mancktelow, N. (2019). Initiation and development of the Pennine Basal Thrust (Swiss Alps): A structural and geochronological study of an exhumed megathrust. *Journal of Structural Geology*, *126*, 338–356. https://doi.org/10.1016/j.jsg.2019.06.014

Caron, J. M. (1994). Metamorphism and deformation in Alpine Corsica. *Schweizerische Mineralogische und Petrographische Mitteilungen*, *74*, 105–114.

Caron, J. M., Kienast, J. R., & Triboulet, C. (1981). High-pressure-low-temperature metamorphism and polyphase alpine deformation at Sant'Andrea di Cotone (eastern Corsica, France). *Tectonophysics*, *78*, 419–451. https://doi.org/10.1016/0040-1951(81)90023-8

Caron, J. M., & Péquignot, G. (1986). The transition beetween blue-schist and lawsonite bearing eclogites on the example of corsican metabasalt. *Lithos*, *19*, 205–218. https://doi.org/10.1016/0024-4937(86)90023-X

Castonguay, S., Ruffet, G., & Tremblay, A. (2007). Dating polyphase deformation across low-grade metamorphic belts: An example based on $^{40}Ar/^{39}Ar$ muscovite age constraints from the southern Quebec Appalachians, Canada. *Geological Society of America Bulletin*, *119*(7–8), 978–992. https://doi.org/10.1130/B26046.1

Cavazza, W., DeCelles, P. G., Fellin, M. G., & Paganellin, L. (2007). The Miocene Saint-Florent Basin in northern Corsica: Stratigraphy, sedimentology, and tectonic implications. *Basin Research*, *19*(4), 507–527. https://doi.org/10.1111/j.1365-2117.2007.00334.x

Cavazza, W., Zattin, M., Ventura, B., & Zuffa, G. G. (2001). Apatite fission-track analysis of Neogene exhumation in northern Corsica (France). *Terra Nova*, *13*, 51–57. https://doi.org/10.1046/j.1365-3121.2001.00316.x

Charles, N., Augier, R., Gumiaux, C., Monié, P., Chen, Y., Faure, M., & Zhu, R. (2013). Timing, duration and role of magmatism in wide rift systems: Insights from the Jiaodong Peninsula (China, East Asia). *Gondwana Research*, *24*, 412–428. https://doi.org/10.1016/j.gr.2012.10.011

Condon, D. J., Hodges, K. V., Alsop, G. I., & White, A. (2006). Laser ablation $^{40}Ar/^{39}Ar$ dating of metamorphic fabrics in the Caledonides of north Ireland. *Journal of the Geological Society, London*, *163*, 337–345. https://doi.org/10.1144/0016-764904-066

Cosca, M., Stunitz, H., Bourgeix, A.-L., & Lee, J. P. (2011). $^{40}Ar^*$ loss in experimentally deformed muscovite and biotite with implications for $^{40}Ar/^{39}Ar$ geochronology of naturally deformed rocks. *Geochimica et Cosmochimica Acta*, *75*, 7759–7778. https://doi.org/10.1016/j.gca.2011.10.012

Dahl, P. (1996). The crystal chemical basis for Ar retention in micas: Inferences from interlayer partitioning and implications for geochronology. *Contributions to Mineralogy and Petrology*, *123*, 22–39. https://doi.org/10.1007/s004100050141

Daniel, J. M., Jolivet, L., Goffé, B., & Poinssot, C. (1996). Crustal-scale strain partitioning: Footwall deformation below the Alpine Oligo-Miocene detachment of Corsica. *Journal of Structural Geology*, *18*(1), 41–59. https://doi.org/10.1016/0191-8141(95)00075-O

Danisik, M., Kuhlemann, J., Dunkl, I., Székely, B., & Frisch, W. (2007). Burial and exhumation of Corsica (France) in the light of fission track data. *Tectonics*, *26*, TC1001. https://doi.org/10.1029/2005TC001938

De Wever, P., Danelian, T., Durand-Delga, M., Cordey, F., & Kito, N. (1987). Datations des radiolarites post-ophiolitiques de Corse alpine à l'aide des radiolaires. *Comptes Rendus de l'Academie Des Sciences de Paris*, *305*, 893–900.

Dempster, T. J. (1992). Zoning and recrystallization of phengitic micas: Implications for metamorphic equilibration. *Contributions to Mineralogy and Petrology*, *109*(4), 526–537. https://doi.org/10.1007/BF00306554

Di Vincenzo, G., Ghiribelli, B., Giorgetti, G., & Palmeri, R. (2001). Evidence of a close link between petrology and isotope records: Constraints from SEM, EMP, TEM and in situ ^{40}Ar-^{39}Ar laser analyses on multiple generations of white micas (Lanterman Range, Antartica). *Earth and Planetary Science Letters*, *192*, 389–405. https://doi.org/10.1016/S0012-821X(01)00454-X

Di Vincenzo, G., Grande, A., Prosser, G., Cavazza, W., & DeCelles, P. G. (2016). ^{40}Ar–^{39}Ar laser dating of ductile shear zones from Central Corsica (France): Evidence of Alpine (middle to late Eocene) syn-burial shearing in Variscan granitoids. *Lithos*, *262*, 369–383. https://doi.org/10.1016/j.lithos.2016.07.022

Di Vincenzo, G., Rocchi, S., Rossetti, F., & Storti, F. (2004). ^{40}Ar-^{39}Ar dating of pseudotachylytes: The effect of clast-hosted extraneous argon in Cenozoic fault-generated friction melts from the West Antarctic Rift System. *Earth and Planetary Science Letters*, *223*, 349–364. https://doi.org/10.1016/j.epsl.2004.04.042

Di Vincenzo, G., Tonarini, S., Lombardo, B., Castelli, D., & Ottolini, L. (2006). Comparison of ^{40}Ar–^{39}Ar and Rb–Sr data on phengites from the UHP Brossasco–Isasca unit (Dora Maira massif, Italy): Implications for dating white mica. *Journal of Petrology*, *47*(7), 1439–1465. https://doi.org/10.1093/petrology/egl018

Di Vincenzo, G., Viti, C., & Rocchi, S. (2003). The effect of chlorite interlayering on ^{40}Ar-^{39}Ar biotite dating: An ^{40}Ar-^{39}Ar laser-probe and TEM investigations of variably chloritised biotites. *Contributions to Mineralogy and Petrology*, *145*(6), 643–658. https://doi.org/10.1007/s00410-003-0472-z

Duchêne, S., Aïssa, R., & Vanderhaeghe, O. (2006). Pressure-temperature-time evolution of metamorphic rocks from Naxos (Cyclades, Greece): Constraints from thermobarometry and Rb/Sr dating. *Geodinamica Acta*, *19*(5), 299–313.

Dunlap, W. J., Teyssier, C., McDougall, I., & Baldwin, S. (1991). Ages of deformation from K/Ar and $^{40}Ar/^{39}Ar$ dating of white micas. *Geology*, *19*(12), 1213–1216. https://doi.org/10.1130/0091-7613(1991)019<1213:AODFKA>2.3.CO;2

Dunlap, W. J. (1997). Neocrystallization or cooling? $^{40}Ar/^{39}Ar$ ages of white micas from low-grade mylonites. *Chemical Geology*, *143*, 181–203. https://doi.org/10.1016/S0009-2541(97)00113-7

Dunlap, W. J., & Kronenberg, A. K. (2001). Argon loss during deformation of micas: Constraints from laboratory deformation experiments. *Contributions to Mineralogy and Petrology*, *141*, 174–185. https://doi.org/10.1007/s004100000217

Etheridge, M. A., Paterson, M. S., & Hobbs, B. E. (1974). Experimentally produced preferred orientation in synthetic mica aggragates. *Contributions to Mineralogy and Petrology*, *44*, 275–294. https://doi.org/10.1007/BF00371557

Fellin, M. G., Vance, J. A., Garver, J. I., & Zattin, M. (2006). The thermal evolution of Corsica as recorded by zircon fission-tracks. *Tectonophysics*, *421*, 299–317. https://doi.org/10.1016/j.tecto.2006.05.001

Ferrandini, J., Ferrandini, M., Rossi, P., & Savary-Sismondini, B. (2010). Définition et datation de la Formation de Venaco (Corse): dépôt d'origine gravitaire d'âge Priabonien. *Comptes Rendus Geoscience*, *342*, 921–929. https://doi.org/10.1016/j.crte.2010.10.002

Ferrandini, J., Gattacceca, J., Ferrandini, M., Deino, A., & Janin, M.-C. (2003). Chronostratigraphie et paléomagnétisme des dépôts oligo-miocènes de Corse: implications géodynamiques pour l'ouverture du bassin liguro-provençal. *Bulletin de la Societe Geologique de France*, *174*(4), 357–371.

Fournier, M., Jolivet, L., Goffé, B., & Dubois, R. (1991). Alpine Corsica metamorphic core complex. *Tectonics*, *10*(6), 1173–1186. https://doi.org/10.1029/91TC00894

Fusseis, F., & Handy, M. R. (2008). Micromechanisms of shear zone propagation at the brittle–viscous transition. *Journal of Structural Geology*, *30*, 1242–1253. https://doi.org/10.1016/j.jsg.2008.06.005

Fusseis, F., Handy, M. R., & Schrank, C. (2006). Networking of shear zones at the brittle-to-viscous transition (Cap de Creus, NE Spain). *Journal of Structural Geology*, *28*, 1228–1243. https://doi.org/10.1016/j.jsg.2006.03.022

Gibbons, W., & Horak, J. (1984). Alpine metamorphim of Hercynian hornblende granodiorite beneath the blueschist facies schistes-lustrés nappe of NE Corsica. *Journal of Metamorphic Geology*, *2*, 95–113. https://doi.org/10.1111/j.1525-1314.1984.tb00290.x

Goodwin, L. B., & Renne, P. R. (1991). Effects of progressive mylonitization on Ar retention in biotites from the Santa Rosa mylonite zone, California, and thermochronologic implications. *Contributions to Mineralogy and Petrology*, *108*, 283–297. https://doi.org/10.1007/BF00285937

Gueydan, F., Brun, J.-P., Phillippon, M., & Noury, M. (2017). Sequential extension as a record of Corsica rotation during Apennines slab roll-back. *Tectonophysics*, *710–711*, 149–161. https://doi.org/10.1016/j.tecto.2016.12.028

Gueydan, F., Leroy, Y. M., Jolivet, L., & Agard, P. (2003). Analysis of continental midcrustal strain localization induced by microfracturing and reaction-softening. *Journal of Geophysical Research*, *108*(B2), 2064. https://doi.org/10.1029/2001JB000611

Hames, W. E., & Bowring, S. A. (1994). An empirical evaluation of the argon diffusion geometry in muscovite. *Earth and Planetary Science Letters*, *124*, 161–169. https://doi.org/10.1016/0012-821X(94)00079-4

Hames, W. E., & Cheney, J. T. (1997). On the loss of ^{40}Ar* from muscovite during polymetamorphism. *Geochimica et Cosmochimica Acta*, *61*(18), 3863–3872.

Hames, W. E., Cheney, J. T., & Tracy, R. J. (2008). Single-crystal ^{40}Ar/^{39}Ar age variation in muscovite of the Gassetts schist and associated gneiss, Vermont Appalachians. *American Mineralogist*, *93*, 384–395. https://doi.org/10.2138/am.2008.2641

Harrison, T. M., Célérier, J., Aikman, A. B., Hermann, J., & Heizler, M. T. (2009). Diffusion of ^{40}Ar in muscovite. *Geochimica et Cosmochimica Acta*, *73*, 1039–1051. https://doi.org/10.1016/j.gca.2008.09.038

Harrison, T. M., Duncan, I., & McDougall, I. (1985). Diffusion of ^{40}Ar in biotite: Temperature, pressure and compositional effects. *Geochimica et Cosmochimica Acta*, *49*, 2461–2468. https://doi.org/10.1016/0016-7037(85)90246-7

Hess, J. C., & Lippolt, H. J. (1986). Kinetics of Ar isotopes during neutron irradiation: ^{39}Ar loss from minerals as a source of error in ^{40}Ar/^{39}Ar dating. *Chemical Geology*, *59*, 223–236. https://doi.org/10.1016/0168-9622(86)90073-4

Isik, V., Tekeli, O., & Seyitoglu, G. (2004). The ^{40}Ar/^{39}Ar age of extensional ductile deformation and granitoid intrusion in the northern Menderes core complex: Implications for the initiation of extensional tectonics in western Turkey. *Journal of Asian Earth Sciences*, *23*, 555–566. https://doi.org/10.1016/j.seaes.2003.09.001

Jolivet, L., Daniel, J. M., & Fournier, M. (1991). Geometry and kinematics of extension in Alpine Corsica. *Earth and Planetary Science Letters*, *104*, 278–291. https://doi.org/10.1016/0012-821X(91)90209-Z

Jolivet, L., Dubois, R., Fournier, M., Goffé, B., Michard, A., & Jourdan, C. (1990). Ductile extension in alpine Corsica. *Geology*, *18*, 1007–1010. https://doi.org/10.1130/0091-7613(1990)018<1007:DEIAC>2.3.CO;2

Jolivet, L., Faccenna, C., Goffé, B., Mattei, M., Rossetti, F., Brunet, C., et al. (1998). Midcrustal shear zones in postorogenic extension: Example from the northern Tyrrhenian Sea. *Journal of Geophysical Research*, *103*(B6), 12,123–12,160. https://doi.org/10.1029/97JB03616

Jourdan, C. (1988). *Balagne orientale et massif du Tenda (Corse septentrionale): étude structurale, interprétation des accidents et des déformations, reconstitutions géodynamiques (Thèse de Doctorat)*. Orsay: Université de Paris-Sud.

Kellett, D. A., Warren, C., Larson, K. P., Zwingmann, H., van Staal, C. R., & Rogers, N. (2016). Influence of deformation and fluids on Ar retention in white mica: Dating the Dover Fault, Newfoundland Appalachians. *Lithos*, *254–255*, 1–17. https://doi.org/10.1016/j.lithos.2016.03.003

Kirschner, D. L., Cosca, M. A., Masson, H., & Hunziker, J. C. (1996). Staircase ^{40}Ar/^{39}Ar spectra of fine-grained white mica: Timing and duration of deformation and empirical constraints on argon diffusion. *Geology*, *24*(8), 747–750. https://doi.org/10.1130/0091-7613(1996)024<0747:SAASOF>2.3.CO;2

Kligfield, R., Hunziker, J., Dallmeyer, R. D., & Schamel, S. (1986). Dating of deformation phases using K-Ar and ^{40}Ar/^{39}Ar techniques: Results from the Northern Apennines. *Journal of Structural Geology*, *8*, 781–798. https://doi.org/10.1016/0191-8141(86)90025-8

Kramar, N., Cosca, M. A., Buffat, P.-A., & Baumgartner, L. P. (2003). Stacking fault-enhanced argon diffusion in naturally deformed muscovite. *Geological Society, London, Special Publications*, *220*, 249–260. https://doi.org/10.1144/GSL.SP.2003.220.01.15

Kramar, N., Cosca, M. A., & Hunziker, J. C. (2001). Heterogeneous ^{40}Ar* distributions in naturally deformed muscovite: In situ UV-laser ablation evidence for microstructurally controlled intragrain diffusion. *Earth and Planetary Science Letters*, *192*, 377–388.

Lahondère, D. (1988). Le métamorphisme éclogitique dans les orthogneiss et les métabasites ophiolitiques de la région de Farinole (Corse). *Bulletin de la Societe Geologique de France*, *4*, 579–585.

Lahondère, D., & Guerrot, C. (1997). Datation Sm-Nd du métamorphisme éclogitique en Corse alpine: un argument pour l'existence au Crétacé supérieur d'une zone de subduction active localisée sous le bloc corso-sarde. *Géologie de la France*, *3*, 3–11.

Lee, J. K. W. (1995). Multipath diffusion in geochronology. *Contributions to Mineralogy and Petrology*, *120*, 60–82. https://doi.org/10.1007/BF00311008

Lo, C.-H., Lee, J. K. W., & Onstott, T. C. (2000). Argon release mechanisms of biotite in vacuo and the role of short-circuit diffusion and recoil. *Chemical Geology*, *165*, 135–166. https://doi.org/10.1016/S0009-2541(99)00167-9

Lo, C.-H., & Onstott, T. C. (1989). ^{39}Ar recoil artifacts in chloritized biotite. *Geochimica et Cosmochimica Acta*, *53*, 2697–2711. https://doi.org/10.1016/0016-7037(89)90141-5

Maggi, M., Rossetti, F., Corfu, F., Theye, T., Andersen, T. B., & Faccenna, C. (2012). Clinopyroxene-rutile phyllonites from the East Tenda Shear Zone (Alpine Corsica, France): Pressure-temperature-time constraints to the Alpine reworking of Variscan Corsica. *Journal of the Geological Society*, *169*, 723–732. https://doi.org/10.1144/jgs2011-120

Maggi, M., Rossetti, F., Ranalli, G., & Theye, T. (2014). Feedback between fluid infiltration and rheology along a regional ductile-to-brittle shear zone: The East Tenda Shear Zone (Alpine Corsica). *Tectonics*, *33*, 253–280. https://doi.org/10.1002/2013TC003370

Mailhé, D. (1982). *Application des méthodes de datation ^{40}Ar/^{39}Ar et traces de fission à l'étude du déroulement de l'orogenèse alpine en Corse (Thèse de Doctorat)*. Montpellier: Université des Sciences et Techniques du Languedoc.

Malusà, M. G., Faccenna, C., Baldwin, S. L., Fitzgerald, P. G., Rossetti, F., Balestrieri, M. L., et al. (2015). Contrasting styles of (U)HP rock exhumation along the Cenozoic Adria-Europe plate boundary (Western Alps, Calabria, Corsica). *Geochemistry, Geophysics, Geosystems*, *16*, 1786–1824. https://doi.org/10.1002/2015GC005767

Mares, V. M., & Kronenberg, A. K. (1993). Experimental deformation of muscovite. *Journal of Structural Geology*, *15*(9–10), 1061–1075. https://doi.org/10.1016/0191-8141(93)90156-5

Markley, M. J., Teyssier, C., & Cosca, M. (2002). The relation between grain size and ^{40}Ar/^{39}Ar date for Alpine white mica from the Siviez-Mischabel Nappe, Switzerland. *Journal of Structural Geology*, *24*, 1937–1955. https://doi.org/10.1016/S0191-8141(02)00006-8

Marti, S., Stünitz, H., Heilbronner, R., Plümper, O., & Drury, M. (2017). Experimental investigation of the brittle-viscous transition in mafic rocks—Interplay between fracturing, reaction, and viscous deformation. *Journal of Structural Geology*, *105*, 62–79. https://doi.org/10.1016/j.jsg.2017.10.011

Martin, L. A. J., Rubatto, D., Brovarone, A. V., & Hermann, J. (2011). Late Eocene lawsonite-eclogite facies metasomatism of a granulite sliver associated to ophiolites in Alpine Corsica. *Lithos*, *125*(1–2), 620–640. https://doi.org/10.1016/j.lithos.2011.03.015

Mattauer, M., Faure, M., & Malavieille, J. (1981). Transverse lineation and large-scale structures related to Alpine obduction in Corsica. *Journal of Structural Geology*, *3*(4), 401–409. https://doi.org/10.1016/0191-8141(81)90040-7

Molli, G., & Malavieille, J. (2011). Orogenic processes and the Corsica/Apennines geodynamic evolution: Insights from Taiwan. *International Journal of Earth Sciences*, *100*, 1207–1224. https://doi.org/10.1007/s00531-010-0598-y

Molli, G., & Tribuzio, R. (2004). Shear zones and metamorphic signature of subducted continental crust as tracers of the evolution of the Corsica/Northern Apennine orogenic system. *Geological Society, London, Special Publications*, *224*(1), 321–335. https://doi.org/10.1144/GSL.SP.2004.224.01.20

Molli, G., Tribuzio, R., & Marquer, D. (2006). Deformation and metamorphism at the eastern border of the Tenda massif (NE Corsica): A record of subduction and exhumation of continental crust. *Journal of Structural Geology*, *28*, 1748–1766. https://doi.org/10.1016/j.jsg.2006.06.018

Monié, P. (1990). Preservation of Hercynian $^{40}Ar/^{39}Ar$ ages through high-pressure low-temperature Alpine metamorphism in the Western Alps. *European Journal of Mineralogy*, *2*, 343–361. https://doi.org/10.1127/ejm/2/3/0343

Mulch, A., Cosca, M. A., & Handy, M. R. (2002). In-situ UV-laser $^{40}Ar/^{39}Ar$ geochronology of a micaceous mylonite: An example of defect-enhanced argon loss. *Contributions to Mineralogy and Petrology*, *142*, 738–752. https://doi.org/10.1007/s00410-001-0325-6

Mulch, A., & Cosca, M. A. (2004). Recrystallization or cooling ages: In situ UV-laser $^{40}Ar/^{39}Ar$ geochronology of muscovite in mylonitic rocks. *Journal of the Geological Society*, *161*, 573–582.

Nardi, R., Puccinelli, A., & Verani, M. (1978). Carta geologica della Balagne «sedimentaria» (Corsica) alla scala 1:25 000 e note illustrative. *Bollettino della Societa Geologica Italiana*, *97*, 3–22.

Ohnenstetter, M., Ohnenstetter, D., Vidal, P., Cornichet, J., Hermitte, D., & Mace, J. (1981). Crystallization and age of zircon from Corsican ophiolitic albitites: Consequences for oceanic expansion in Jurassic times. *Earth and Planetary Science Letters*, *54*, 397–408. https://doi.org/10.1016/0012-821X(81)90056-X

Oriolo, S., Wemmer, K., Oyhantçabal, P., Fossen, H., Schulz, B., & Siegesmund, S. (2018). Geochronology of shear zones—A review. *Earth-Science Reviews*, *185*, 665–683. https://doi.org/10.1016/j.earscirev.2018.07.007

Pec, M., Stünitz, H., & Heilbronner, R. (2012). Semi-brittle deformation of granitoid gouges in shear experiments at elevated pressures and temperatures. *Journal of Structural Geology*, *38*, 200–221. https://doi.org/10.1016/j.jsg.2011.09.001

Putlitz, B., Cosca, M. A., & Schumacher, J. C. (2005). Prograde mica $^{40}Ar/^{39}Ar$ growth ages recorded in high pressure rocks (Syros, Cyclades, Greece). *Chemical Geology*, *214*(1–2), 79–98. https://doi.org/10.1016/j.chemgeo.2004.08.056

Ravna, E. J. K., Andersen, T. B., Jolivet, L., & De Capitani, C. (2010). Cold subduction and the formation of lawsonite eclogite—Constraints from prograde evolution of eclogitized pillow lava from Corsica. *Journal of Metamorphic Geology*, *28*, 381–395. https://doi.org/10.1111/j.1525-1314.2010.00870.x

Renne, P. R., Swisher, C. C., Deino, A. L., Karner, D. B., Owens, T. L., & DePaolo, D. J. (1998). Intercalibration of standards, absolute ages abd uncertainties in $^{40}Ar/^{39}Ar$ dating. *Chemical Geology*, *145*, 117–152. https://doi.org/10.1016/S0009-2541(97)00159-9

Rolland, Y., Alexeiev, D. V., Kröner, A., Corsini, M., Loury, C., & Monié, P. (2013). Late Palaeozoic to Mesozoic kinematic history of the Talas–Ferghana strike-slip fault (Kyrgyz West Tianshan) as revealed by $^{40}Ar/^{39}Ar$ dating of syn-kinematic white mica. *Journal of Asian Earth Sciences*, *67–68*, 76–92. https://doi.org/10.1016/j.jseaes.2013.02.012

Rolland, Y., Cox, S. F., & Corsini, M. (2009). Constraining deformation stages in brittle–ductile shear zones from combined field mapping and $^{40}Ar/^{39}Ar$ dating: The structural evolution of the Grimsel Pass area (Aar massif, Swiss Alps). *Journal of Structural Geology*, *31*(11), 1377–1394. https://doi.org/10.1016/j.jsg.2009.08.003

Rossetti, F., Glodny, J., Theye, T., & Maggi, M. (2015). Pressure-temperature-deformation-time of the ductile Alpine shearing in Corsica: From orogenic construction to collapse. *Lithos*, *218–219*, 99–116. https://doi.org/10.1016/j.lithos.2015.01.011

Rossi, P., Durand-Delga, M., Caron, J. M., Guieu, G., Conchon, O., Libourel, G., & Loÿe-Pilot, M.-D. (1994). Carte Géologique de France (1/50000), feuille de Corte (1110). Bureau des Recherches Géologiques et Minières.

Rossi, P., Durand-Delga, M., & Cocherie, A. (1993). Caractère volcano-plutonique du magmatisme calco-alcalin composite d'âge Stéphanien supérieur-Permien inférieur en Corse. *Comptes Rendus de l'Academie Des Sciences de Paris*, *316*, 1779–1788.

Rossi, P., Durand-Delga, M., Lahondère, J.-C., Baud, J.-P., Egal, E., Lahondère, D., et al. (2001). Carte Géologique de France (1/50 000), feuille de Santo-Pietro-Di-Tenda (1106). Bureau des Recherches Géologiques et Minières.

Rossi, P., Lahondère, J.-C., Lluch, D., Loÿe-Pilot, M.-D., & Jacquet, M. (1994). Carte Géologique de France (1/50 000), feuille de Saint-Florent (1103). Bureau des Recherches Géologiques et Minières.

Sanchez, G., Rolland, Y., Schneider, J., Corsini, M., Oliot, E., Goncalves, P., et al. (2011). Dating low-temperature deformation by $^{40}Ar/^{39}Ar$ on white mica, insights from the Argentera-Mercantour massif (SW Alps). *Lithos*, *125*, 521–536. https://doi.org/10.1016/j.lithos.2011.03.009

Scaillet, S. (1996). Excess ^{40}Ar transport scale and mechanism in high-pressure phengites: A case study from an eclogitized metabasite of the Dora-Maira nappe, western Alps. *Geochimica et Cosmochimica Acta*, *60*(6), 1075–1090. https://doi.org/10.1016/0016-7037(95)00440-8

Scaillet, S. (1998). K-Ar ($^{40}Ar/^{39}Ar$) geochronology of ultrahigh pressure rocks. In B. R. Hacker & J. G. Liou (Eds.), *When continents collide: Geodynamics and geochemistry of ultrahigh-pressure rocks* (pp. 161–201). Dordrecht: Kluwer.

Scaillet, S. (2000). Numerical error analysis in $^{40}Ar/^{39}Ar$ dating. *Chemical Geology*, *162*, 269–298. https://doi.org/10.1016/S0009-2541(99)00149-7

Scaillet, S., Feraud, G., Ballevre, M., & Amouric, M. (1992). Mg/Fe and [(Mg,Fe)Si-Al_2] compositional control on argon behaviour in high-pressure white micas: A $^{40}Ar/^{39}Ar$ continuous laser-probe study from the Dora-Maira nappe of the internal western Alps, Italy. *Geochimica et Cosmochimica Acta*, *56*(7), 2851–2872. https://doi.org/10.1016/0016-7037(92)90364-O

Scaillet, S., Féraud, G., Lagabrielle, Y., Ballèvre, M., & Ruffet, G. (1990). $^{40}Ar/^{39}Ar$ laser-probe dating by step heating and spot fusion of phengites from the Dora Maira nappe of the western Alps, Italy. *Geology*, *18*, 741–744. https://doi.org/10.1130/0091-7613(1990)018<0741:AALPDB>2.3.CO;2

Scaillet, S., Vita-Scaillet, G., & Rotolo, S. G. (2013). Millennial-scale phase relationships between ice-core and Mediterranean marine records: Insights from high-precision $^{40}Ar/^{39}Ar$ dating of the Green Tuff of Pantelleria, Sicily Strait. *Quaternary Science Reviews*, *78*, 141–154. https://doi.org/10.1016/j.quascirev.2013.08.008

Schärer, U., Zhang, L.-S., & Tapponnier, P. (1994). Duration of strike-slip movements in large shear zones: The Red River belt, China. *Earth and Planetary Science Letters*, *126*, 379–397. https://doi.org/10.1016/0012-821X(94)90119-8

Scharf, A., Handy, M. R., Schmid, S. M., Favaro, S., Sudo, M., Schuster, R., & Hammerschmidt, K. (2016). Grain-size effects on the closure temperature of white mica in a crustal-scale extensional shear zone—Implications of in-situ $^{40}Ar/^{39}Ar$ laser-ablation of white mica for dating shearing and cooling (Tauern Window, Eastern Alps). *Tectonophysics*, *674*, 210–226. https://doi.org/10.1016/j.tecto.2016.02.014

Schneider, S., Hammerschmidt, K., & Rosenberg, C. L. (2013). Dating the longevity of ductile shear zones: Insight from $^{40}Ar/^{39}Ar$ in situ analyses. *Earth and Planetary Science Letters*, *369–370*, 43–58. https://doi.org/10.1016/j.epsl.2013.03.0023.3

Smye, A. J., Warren, C. J., & Bickle, M. J. (2013). The signature of devolatisation: Extraneous ^{40}Ar systematics in high-pressure metamorphic rocks. *Geochimica et Cosmochimica Acta*, *113*, 94–112. https://doi.org/10.1016/j.gca.2013.03.018

Stockli, D. F. (2005). Application of low-temperature thermochronometry to extensional tectonic settings. *Reviews in Mineralogy and Geochemistry*, *58*, 411–448. https://doi.org/10.2138/rmg.2005.58.16

Tribuzio, R., & Giacomini, F. (2002). Blueschist facies metamorphism of peralkaline rhyolites from the Tenda crystalline massif (northern Corsica): Evidence for involvement in the Alpine subduction event? *Journal of Metamorphic Geology*, *20*(5), 513–526. https://doi.org/10.1046/j.1525-1314.2002.00382.x

Turrillot, P., Augier, R., Monié, P., & Faure, M. (2011). Late orogenic exhumation of the Variscan high-grade units (South Armorican Domain, western France), combined structural and ^{40}Ar/^{39}Ar constraints. *Tectonics*, *30*, TC5007. https://doi.org/10.1029/2010tc002788

Vernon, R. H. (1977). Microfabric of mica aggregates in partly recrystallized biotite. *Contributions to Mineralogy and Petrology*, *61*, 175–185. https://doi.org/10.1007/BF00374366

Vitale Brovarone, A., Beltrando, M., Malavieille, J., Giuntoli, F., Tondella, E., Groppo, C., et al. (2011). Inherited ocean-continent transition zones in deeply subducted terranes: Insights from Alpine Corsica. *Lithos*, *124*, 273–290. https://doi.org/10.1016/j.lithos.2011.02.013

Vitale Brovarone, A., Beyssac, O., Malavieille, J., Molli, G., Beltrando, M., & Compagnoni, R. (2013). Stacking and metamorphism of continuous segments of subducted lithosphere in a high-pressure wedge: The example of Alpine Corsica (France). *Earth-Science Reviews*, *116*, 35–56. https://doi.org/10.1016/j.earscirev.2012.10.003

Vitale Brovarone, A., Groppo, C., Hetényi, G., Compagnoni, R., & Malavieille, J. (2011). Coexistence of lawsonite-bearing eclogite and blueschist: Phase equilibria modelling of Alpine Corsica metabasalts and petrological evolution of subducting slabs. *Journal of Metamorphic Geology*, *29*(5), 583–600. https://doi.org/10.1111/j.1525-1314.2011.00931.x

Vitale Brovarone, A., & Herwartz, D. (2013). Timing of HP metamorphism in the Schistes Lustrés of Alpine Corsica: New Lu-Hf garnet and lawsonite ages. *Lithos*, *172*, 175–191. https://doi.org/10.1016/j.lithos.2013.03.009

Warren, C. J., Hanke, F., & Kelley, S. P. (2012). When can muscovite ^{40}Ar/^{39}Ar dating constrain the timing of metamorphic exhumation? *Chemical Geology*, *291*, 79–86. https://doi.org/10.1016/j.chemgeo.2011.09.017

West, D. P., & Hubbard, M. S. (1997). Progressive localization of deformation during exhumation of a major strike-slip shear zone: Norumbega fault zone, south-central Maine, USA. *Tectonophysics*, *273*, 185–201.

West, D. P., & Lux, D. R. (1993). Dating mylonitic deformation by the ^{40}Ar-^{39}Ar method: An example from the Norumbega Fault Zone, Maine. *Earth and Planetary Science Letters*, *120*, 221–237.

Wijbrans, J. R., & McDougall, I. (1986). ^{40}Ar/^{39}Ar dating of white micas from an Alpine high-pressure metamorphic belt on Naxos (Greece): The resetting of the argon isotopic system. *Contributions to Mineralogy and Petrology*, *93*, 187–194. https://doi.org/10.1007/BF00371320

Wilson, C. J. L., & Bell, I. A. (1979). Deformation of biotite and muscovite: Optical microstructure. In: Bell, T. H., Vernon, R. H. (Eds.), Microstructural processes during deformation and metamorphism. *Tectonophysics*, *58*(1–2), 179–200. https://doi.org/10.1016/0040-1951(79)90328-7

Zarki-Jakni, B., van der Beek, P., Poupeau, G., Sosson, M., Labrin, E., Rossi, P., & Ferrandini, J. (2004). Cenozoic denudation of Corsica in response to Ligurian and Tyrrhenian extension: Results from apatite fission track thermochronology. *Tectonics*, *23*, TC1003. https://doi.org/10.1029/2003TC001535